공학석사학위논문

Novel Mitigation Methods of Lever Arm Effect in Redundant Inertial Measurement Units

중첩 관성 센서에서 레버암 효과 완화의 새로운 기법

2021년 2월

서울대학교 대학원
항공우주공학과

조 용 현

Novel Mitigation Methods of Lever Arm Effect in Redundant Inertial Measurement Units

중첩 관성 센서에서 레버암 효과 완화의 새로운 기법

지도교수 박 찬 국

이 논문을 공학석사 학위논문으로 제출함

2020 년 12 월

서울대학교 대학원

항공우주공학과

조 용 현

조용현의 공학석사 학위논문을 인준함

2020 년 12 월

위 원 장 _____ (인)

부위원장 _____ (인)

위 원 _____ (인)

Abstract

Novel Mitigation Methods of Lever Arm Effect in Redundant Inertial Measurement Units

Yong Hyeon Cho
Department of Aerospace Engineering
The Graduate School
Seoul National University

This master's thesis presents two novel methods to mitigate lever arm effect in Redundant Inertial Measurement Units (RIMUs), each with different approaches. With the presence of a lever arm for each sensing axis, the unexpected accelerations such as Euler and centrifugal accelerations are added to the measurements through rotational motion, resulting in an estimation error of linear acceleration. Therefore, it was previously considered as the best option to minimize the length of the lever arm and compensate the lever arm effect from the accelerometer measurements. However, this approach cannot completely remove the estimation error as the compensated value is based on the estimated angular rates, where the magnitude of the error becomes more apparent with a RIMU composed of low-grade gyroscopes that shows a higher noise level. In order to solve this problem, we propose two methods that can mitigate estimation error using the specific arrangement of the lever arm vectors and the concentrated

likelihood method-based nonlinear least squares (NLS). By the proposed methods, the accuracy in compensating the lever arm effect can be increased by placing the lever arm vectors symmetrically or using the information from accelerometers when estimating angular rates. Besides, the suggested methods each have their own advantages in computational efficiency and overall navigation performance, compared to previous method. The effectiveness of the proposed methods is verified through simulations including misalignments of each redundant sensor.

Keywords: Inertial navigation, Redundant inertial measurement units, Lever arm, Concentrated likelihood method, Optimal navigation performance

Student number: 2019-29291

Contents

List of Tables

List of Figures

Chapter 1

Introduction

1.1 Motivation and background

Inertial navigation system (INS) is a self-contained system since the navigation process does not depend on signals from the vehicle or reception from other sources [1]. Based on the linear acceleration and angular velocity measured at a high sampling rate by Inertial Measurement Units (IMUs), the position, velocity, and attitude of the body frame on which the IMU is installed are calculated seamlessly over time. Due to these characteristics, it has a wide range of uses, from space navigation to pedestrian dead reckoning (PDR).

Meanwhile, as more accurate and reliable navigation performance is required, the concept of redundant IMU (RIMU) has emerged where more measurements are utilized from additional IMUs. The redundancy improves navigation performance based on RIMU's acceleration and angular velocity estimates and allows on-line failure detection and fail-safe operation [2]. However, since the advantages of using RIMU are dependent on the orientation of sensing axes, numerous research has been conducted on the optimal configuration of extra sensors.

The linear acceleration and angular rate of RIMU are estimated from measurement equations where the Jacobian matrix of it consists of n row vectors, each of which is a dot product of the sensing axis direction and the unit vector of

the RIMU frame [3]. Since the estimates of accelerations or angular rates are based on the least squares (LS) method, the optimal configuration that can minimize the estimation error is required. Therefore, various types of figure of merit (FOM), which characterize the estimation error covariance $\mathbf{P}$, have been introduced as a cost function to be minimized. The most commonly used FOM is $\det(\mathbf{P})$ [3], [4], representing the volume of error ellipsoid. There are also other forms of FOM, such as trace of the error covariance matrix ($\mathrm{Tr}(\mathbf{P})$) [5], which represents the geometric dilution of precision (GDOP), or the maximum eigenvalue of the error covariance matrix ($\lambda_{\max}(\mathbf{P})$) [6], which stands for the worst-case estimation.

Although all of these FOMs differ slightly in terms of the sensitivity of the cost function values, the mathematical meaning behind them is fundamentally identical, yielding the same results. Eventually, the constraint expressed by Eq. (1.1) must be satisfied in order to minimize the estimation error as much as possible, where n is the number of redundant sensing axes, $\mathbf{H}$ is the Jacobian matrix of measurement equation, and $\mathbf{I}_{3\times3}$ stands for the 3-dimensional identity matrix.

$$\left(\mathbf{H}^{\mathrm{T}}\mathbf{H}\right)^{-1} = \frac{3}{n}\mathbf{I}_{3\times3} \tag{1.1}$$

Depending on the number of redundant sensors, the determination of the sensing axes orientation satisfying Eq. (1.1) can be set based on the conical shape or platonic solid. Various optimal configuration can be referred to [7]–[12].

The fault detection and isolation (FDI) algorithms are based on the parity equations which reflect the failure status of the sensors. There are various ways to detect faults and isolate erroneous sensors from RIMUs such as generalized likelihood test (GLT) [13], [14], sequential analysis [15], squaresd-error analysis

[16], minimax analysis [17], Mahalanobis distance [18], wavelet transform based method [19] and so on.

The ability of FDI performance is also affected by the configuration of sensing axes. Shim [8] suggested a cost function that finds the largest angle between the closest sensing axes to find the optimal configuration for FDI among the configurations satisfying Eq. (1.1). The probability of correct isolation (PCI) was confirmed by Monte Carlo simulation, and the results are also consistent with the results in [3].

1.2 Objectives and contributions

As described above, based on the navigation performance and FDI performance, most of the previous works on RIMU has focused on the optimal configuration of sensing axes orientation. However, when designing an actual RIMU unit, consideration of the lever arm of each sensing axis is inevitable because of the physical size of redundant IMU. The illustration of lever arm vector $\mathbf{d}_i$ is described in Figure 1.1, where the physical size of each sensor is depicted as a sphere.

The effect of the lever arm is represented by Euler and centrifugal forces, which are the latter two terms of nonlinear equation Eq. (1.2).

$$f_i = \mathbf{h}_i \cdot \left\{ \mathbf{f} + \dot{\boldsymbol{\omega}} \times \mathbf{d}_i + \boldsymbol{\omega} \times \left(\boldsymbol{\omega} \times \mathbf{d}_i \right) \right\} \tag{1.2}$$

$$\omega_i = \mathbf{h}_i \cdot \boldsymbol{\omega} \tag{1.3}$$

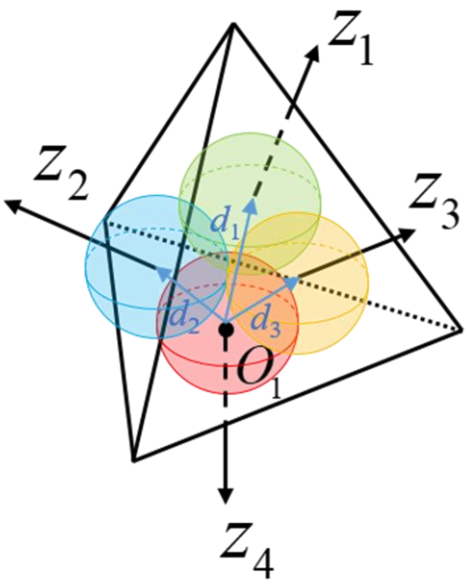

Figure 1.1: Traditional tetrahedron configuration considering the lever arms

where i is the index for the redundant sensors consists of multiple accelerometers and gyroscopes. $\mathbf{f}$, $\boldsymbol{\omega}$, and $\dot{\boldsymbol{\omega}}$ each stands for linear acceleration, angular rate, and angular acceleration of the RIMU. $\mathbf{d}_i$ represents the lever arm that belongs to the ith sensor.

For the application of RIMU in the long term navigation such as ship or airplane, the angular rate or angular acceleration of the body frame can be regarded as zero for most of the time. In those cases, it is valid to neglect the latter two terms in Eq. (1.2) for estimating the accelerations by LS. However, maneuverings of land vehicles or unmanned aerial vehicle (UAV) often contain some amount of angular motion, making the lever arm effect in Eq. (1.2) non-negligible. Therefore, if the conventional LS is applied without considering the lever arm effect, an estimation error will occur, and navigation performance will deteriorate.

So far, the best way to minimize the estimation error induced by the lever arm effect is addressed by the optimal allocation of lever arm vectors [6]. The minimum length and direction of lever arms for the case of four and five sensing axes is addressed in an optimal manner by assuming the size of each redundant sensors as a sphere of radius r. However, the optimization problem of assigning each lever arm vector becomes complex as the number of sensing axes increases, and different solutions can be obtained depending on how the physical shape of each sensor is assumed. Moreover, there still remains the estimation error with the optimized solution, since the lever arm effect to be compensated are based on the angular rates estimated from the noisy measurements.

In this thesis, two methods are proposed to mitigate the lever arm effect with the presence of the multiple lever arms. One way is to cancel the lever arm effect using the specific configuration of the lever arm. By making multiple pairs of the sensing axes with the same orientation to each other have the lever arm vectors in the opposite direction, the summation of multiple nonlinear measurement equations falls into a single linear equation where lever arm effects are excluded. The other way uses concentrated likelihood method-based NLS on the lever arm of orientation parallel to its corresponding sensing axis.

By following these methods, the estimation of acceleration is no longer affected by the turning motion, which leads to the enhancement in the navigation performance. Since the navigation performance of both methods does not depend on the length of the lever arm, it frees the burden of designing the optimal configuration of the lever arm vector when designing RIMU sensors.

Chapter 2

Related Works

2.1 Inertial navigation system

Inertial Navigation System (INS) calculates vehicle's position, velocity, and attitude based on the output from Inertial Measurement Units (IMU), which is usually composed of a 3-axis accelerometer and a gyroscope, where each of the sensing axis is orthogonal to each other. Since the IMU has a high sampling rate, it leads to a seamless navigation by the principle of Dead Reckoning (DR) method. However, it also has the characteristics that the navigation error can diverge rapidly as the time goes by, and its navigation performance is sensitive to the initial error such as position error, velocity error, tilt error, and azimuth error.

In this section, mechanization of the frame which the vehicle navigates through is firstly introduced. The navigation equations based on the various reference frames are derived including Earth Centered Inertial (ECI) frame, Earth Centered Earth Fixed (ECEF) frame, and local geographic navigation frame, starting from the fundamental navigation equation. Then, the process of calculating attitude, velocity, and position is addressed, step by step on the principle of kinematics. Base on the kinematic equations, the error equations is also derived in order to analyze the inertial navigation performance.

2.1.1 Frame mechanization

The kinematics related to navigation can be differed by the reference frame. Starting from the ECI frame where its center is located on the center of the earth, the differential equations about velocity with respect to the observer located on the earth are derived on the ECEF, and local geographic navigation frame.

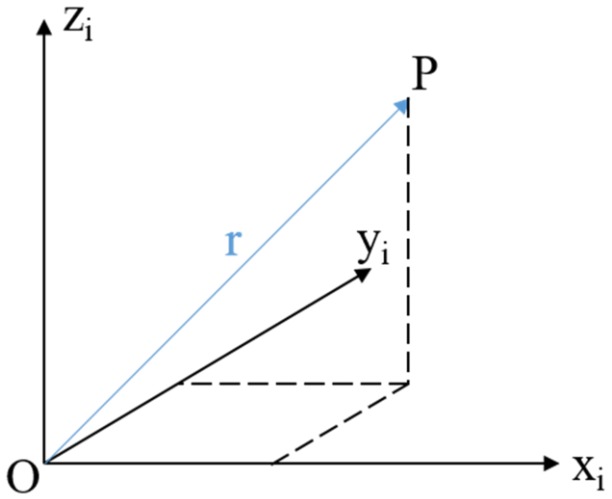

Figure 2.1: Position vector with respect to reference frame

2.1.1.1 Fundamental navigation equation

In order to deal with the kinematics resolved in various frame, a basic equation should be derived for the further process. It is derived by the relation between the measurement outputs from the IMU located on the point P and its acceleration. The point P is located on the ECI reference frame as Figure 2.1

$$\mathbf{f}_{ib} = \left.\frac{d^2\mathbf{r}_{ib}}{dt^2}\right|_i - \mathbf{g} \tag{2.1}$$

The subscript *i* and *b* stands for the inertial frame and body frame respectively. The output of accelerometer is subtracted by the gravity vector from its own acceleration $\left.\frac{d^2\mathbf{r}}{dt^2}\right|_i$, where subscript *i* is the standard frame where the derivatives are drawn.

2.1.1.2 Earth centered inertial frame mechanization

By the principle of Coriolis theorem, derivative of the position with respect to inertial frame can be expressed by the derivative described in ECEF as follows:

$$\left.\frac{d\mathbf{r}_{ib}}{dt}\right|_i = \left.\frac{d\mathbf{r}_{eb}}{dt}\right|_e + \boldsymbol{\omega}_{ie} \times \mathbf{r}_{eb} \tag{2.2}$$

By differentiating both side of the equation with respect to the ECI frame and reorganizing it:

$$\left.\frac{d^2\mathbf{r}_{ib}}{dt^2}\right|_i = \left.\frac{d\mathbf{v}_{eb}}{dt}\right|_i + \boldsymbol{\omega}_{ie} \times \mathbf{v}_{eb} + \boldsymbol{\omega}_{ie} \times \left(\boldsymbol{\omega}_{ie} \times \mathbf{r}_{eb}\right) \tag{2.3}$$

By substituting Eq. (2.1) into Eq. (2.3):

$$\left.\frac{d\mathbf{v}_{eb}}{dt}\right|_i = \mathbf{f}_{ib} - \boldsymbol{\omega}_{ie} \times \mathbf{v}_{eb} + \mathbf{g}_l \tag{2.4}$$

where $\mathbf{g}_l = \mathbf{g} - \boldsymbol{\omega}_{ie} \times \left(\boldsymbol{\omega}_{ie} \times \mathbf{r}_{eb}\right)$, which is also called by plum-bob gravity vector, and $\boldsymbol{\omega}_{ie}$ stands for the earth's rotation. Eq. (2.3) may be resolved in the ECI frame as bellow:

$$\dot{\mathbf{v}}^i_{eb} = \mathbf{C}^i_b \mathbf{f}^b_{ib} - \boldsymbol{\omega}^i_{ie} \times \mathbf{v}^i_{eb} + \mathbf{g}^i_l \tag{2.5}$$

where superscript *i* represents the frame where vectors are resolved. Although Eq. (2.4) is not used often in practical application, it is advantageous in that it is used to derive other following equations.

2.1.1.3 Earth centered earth fixed frame mechanization

Likewise, the derivation starts from the Coriolis theorem, now with its derivative form:

$$\left.\frac{d\mathbf{v}_{eb}}{dt}\right|_e = \left.\frac{d\mathbf{v}_{eb}}{dt}\right|_i - \boldsymbol{\omega}_{ie} \times \mathbf{v}_{eb} \tag{2.6}$$

By substituting Eq. (2.4) into Eq. (2.6):

$$\left.\frac{d\mathbf{v}_{eb}}{dt}\right|_i = \mathbf{f}_{ib} - 2\boldsymbol{\omega}_{ie} \times \mathbf{v}_{eb} + \mathbf{g}_l \tag{2.7}$$

Resolving Eq. (2.7) in the ECEF frame is therefore

$$\dot{\mathbf{v}}^e_{eb} = \mathbf{C}^e_b \mathbf{f}^b_{ib} - 2\boldsymbol{\omega}^e_{ie} \times \mathbf{v}^e_{eb} + \mathbf{g}^e_l \tag{2.8}$$

The ECEF mechanization is useful for the missile guidance, as the ground station from which the tracking information is provided is fixed on the point of the earth. Both the missile and the tracking information from station should be resolved in the same reference. Moreover, for the short term navigation, the Coriolis term in Eq. (2.8) can be neglected and summarized as

$$\dot{\mathbf{v}}^e_{eb} = \mathbf{C}^e_b \mathbf{f}^b_{ib} + \mathbf{g}^e_l \tag{2.9}$$

2.1.1.4 Local geographic navigation frame mechanization

From the derivative form of the Coriolis equation:

$$\left.\frac{d\mathbf{v}_{eb}}{dt}\right|_n = \left.\frac{d\mathbf{v}_{eb}}{dt}\right|_i - \boldsymbol{\omega}_{in} \times \mathbf{v}_{eb} \tag{2.10}$$

By substituting Eq. (2.4) into Eq. (2.10):

$$\left.\frac{d\mathbf{v}_{eb}}{dt}\right|_n = \mathbf{f}_{ib} - \left(2\boldsymbol{\omega}_{ie} + \boldsymbol{\omega}_{en}\right) \times \mathbf{v}_{eb} + \mathbf{g}_l \tag{2.11}$$

where $\boldsymbol{\omega}_{en}$ is the transport rate that describes the angular motion of the local geographic navigation frame caused by the maneuvering over the earth surface. Resolving Eq. (2.11) in the local geographic navigation frame (NED frame):

$$\dot{\mathbf{v}}_{eb}^n = \mathbf{C}_b^n \mathbf{f}_{ib}^b - \left(2\boldsymbol{\omega}_{ie}^n + \boldsymbol{\omega}_{en}^n\right) \times \mathbf{v}_{eb}^n + \mathbf{g}_l^n \tag{2.12}$$

From the point of view in NED frame, $2\boldsymbol{\omega}_{ie}^n \times \mathbf{v}_{eb}^n$ stands for the correction of the Coriolis acceleration which is the effect caused by the vehicle's velocity on the surface of a rotating earth, $\boldsymbol{\omega}_{en}^n \times \mathbf{v}_{eb}^n$ is a correction for the centripetal acceleration of the vehicle. The mechanization derived in NED frame is mostly used in INS, and it describes the kinematics for the long term navigation. In this thesis, the mechanization about NED frame is selected to describe the simulated motion.

2.1.2 Attitude update algorithm

In order to calculate the vehicle's attitude in real time, the change rate of the attitude should be mechanized with respect to time. Each differential equation is derived for Euler angles, Direct Cosine Matrix (DCM), and quaternions, which are three representative methods of representing the vehicle's attitude relative to the

reference frame. The alignment process is also addressed, which is a way to determine the initial attitude.

2.1.2.1 Euler angle

The Euler angles are gimbal angles to be rotated in a specific order to represent the vehicle's attitude, where a gimbal is a mechanical frame that is free to rotate about a single-axis in order to isolate it from angular motion in the same direction. By using DCM, where each of its columns belongs to the projection of a unit vector along the reference axes, rotation with respect to each axes can be shown as bellows:

$$\mathbf{C}_1 = \begin{bmatrix} \cos\psi & \sin\psi & 0 \\ -\sin\psi & \cos\psi & 0 \\ 0 & 0 & 1 \end{bmatrix} \tag{2.13}$$

$$\mathbf{C}_2 = \begin{bmatrix} \cos\theta & 0 & -\sin\theta \\ 0 & 1 & 0 \\ \sin\theta & 0 & \cos\theta \end{bmatrix} \tag{2.14}$$

$$\mathbf{C}_3 = \begin{bmatrix} 1 & 0 & 0 \\ 0 & \cos\phi & \sin\phi \\ 0 & -\sin\phi & \cos\phi \end{bmatrix} \tag{2.15}$$

where ψ is a rotation angle about z-axis, θ is a rotation about y-axis, and ϕ is a rotation about x-axis. If a transformation from reference frame to body frame is defined as

$$\mathbf{C}_n^b = \mathbf{C}_3\mathbf{C}_2\mathbf{C}_1 \tag{2.16}$$

Eq. (2.16) implies that the vector multiplied by $\mathbf{C}_n^b$ is rotated under the order of z, y, and x axis. As the rotation around x-axis is performed at the last order, the propagation of Euler angles with time that transforms reference frame to body frame can be represented as follows:

$$\begin{bmatrix} \omega_x \\ \omega_y \\ \omega_z \end{bmatrix}_{nb} = \begin{bmatrix} \dot{\phi} \\ 0 \\ 0 \end{bmatrix} + \mathbf{C}_3 \begin{bmatrix} 0 \\ \dot{\theta} \\ 0 \end{bmatrix} + \mathbf{C}_3\mathbf{C}_2 \begin{bmatrix} 0 \\ 0 \\ \dot{\psi} \end{bmatrix} \tag{2.17}$$

where $\omega_x, \omega_y, \omega_z$ each stands for the change rate of the rotation vector projected on x, y, and z-axis. Note that Eq. (2.17) is the relation between the change rate of Euler angle and rotation angle that transforms reference frame to body frame. However, when it comes to the application of the navigation, the rotation angle that transforms body frame to reference frame is used typically. As the inversion matrix of $\mathbf{C}_n^b$ can be written as

$$\mathbf{C}_b^n = \mathbf{C}_1^{\mathrm{T}}\mathbf{C}_2^{\mathrm{T}}\mathbf{C}_3^{\mathrm{T}} \tag{2.18}$$

Therefore, the relation between Euler angle and the rotation vector that transforms the body frame to navigation frame is

$$\begin{bmatrix} \omega_x \\ \omega_y \\ \omega_z \end{bmatrix}_{bn} = \mathbf{C}_1^{\mathrm{T}}\mathbf{C}_2^{\mathrm{T}} \begin{bmatrix} \dot{\phi} \\ 0 \\ 0 \end{bmatrix} + \mathbf{C}_1^{\mathrm{T}} \begin{bmatrix} 0 \\ \dot{\theta} \\ 0 \end{bmatrix} + \begin{bmatrix} 0 \\ 0 \\ \dot{\psi} \end{bmatrix} \tag{2.19}$$

Using Eq. (2.19), the error of roll, pitch, yaw is propagated as the following equations

$$\begin{bmatrix}\delta\sigma_x\\ \delta\sigma_y\\ \delta\sigma_z\end{bmatrix} = \mathbf{C}_1^{\mathrm{T}}\mathbf{C}_2^{\mathrm{T}}\begin{bmatrix}\delta\phi\\ 0\\ 0\end{bmatrix} + \mathbf{C}_1^{\mathrm{T}}\begin{bmatrix}0\\ \delta\theta\\ 0\end{bmatrix} + \begin{bmatrix}0\\ 0\\ \delta\psi\end{bmatrix} = \begin{bmatrix}\cos\theta\cos\psi & -\sin\psi & 0\\ \cos\theta\sin\psi & \cos\psi & 0\\ -\sin\theta & 0 & 1\end{bmatrix}\begin{bmatrix}\delta\phi\\ \delta\theta\\ \delta\psi\end{bmatrix} \tag{2.20}$$

Therefore,

$$\begin{bmatrix}\delta\phi\\ \delta\theta\\ \delta\psi\end{bmatrix} = \begin{bmatrix}\sec\theta\cos\psi & \sec\theta\sin\psi & 0\\ -\sin\psi & \cos\psi & 0\\ \tan\theta\cos\psi & \tan\theta\sin\psi & 1\end{bmatrix}\begin{bmatrix}\delta\sigma_x\\ \delta\sigma_y\\ \delta\sigma_z\end{bmatrix} \tag{2.21}$$

where $\delta\sigma_x$, $\delta\sigma_y$, $\delta\sigma_z$ each stands for the error of rotation vector. The propagation of Euler angle is not practically used as Eq. (2.19) is affected by the gimbal lock problem when $\theta = \pm 90^\circ$, where the yawing and rolling cause the change of attitude in the same fashion. However, the error equation derived from Eq. (2.19), which is Eq. (2.21), can be used as a measurement equation for the attitude and heading reference (AHRS) system. Eq. (2.21) also implies that the error propagation behaves differently between rotation vector and Euler angle.

2.1.2.2 Direction cosine matrix

As mentioned above, each column of DCM is composed of unit vectors containing information about direction relationship between body frame and reference frame. The amount of change in $\mathbf{C}_b^n$ during δt can be represented by dividing $\mathbf{C}_{b(t+\delta t)}^{n(t+\delta t)}$ into separate two DCMs:

$$\mathbf{C}_{b(t+\delta t)}^{n(t+\delta t)} = \mathbf{C}_{b(t)}^{n(t+\delta t)}\mathbf{A}(t) \tag{2.22}$$

where $\mathbf{A}(t)$ is a DCM that transforms attitude from the b-frame at time $t+\delta t$ to the b-frame at time t ($\mathbf{C}_{b(t+\delta t)}^{b(t)}$) which regards the b-frame at time t as a reference, and it is also the following result of $\lim_{\phi,\theta,\psi\to 0}\mathbf{C}_b^n$ in Eq. (2.18). Therefore,

$$\mathbf{A}(t) = \mathbf{I} + \delta\boldsymbol{\Psi} \tag{2.23}$$

$$\delta\boldsymbol{\Psi} = \begin{bmatrix} 0 & -\delta\psi & \delta\theta \\ \delta\psi & 0 & -\delta\phi \\ -\delta\theta & \delta\phi & 0 \end{bmatrix} \tag{2.24}$$

As a result, the change rate of $\mathbf{C}_b^n(t)$ is described as

$$\begin{aligned} \dot{\mathbf{C}}_b^n &= \lim_{\delta t\to 0}\frac{\delta\mathbf{C}_b^n}{\delta t} = \lim_{\delta t\to 0}\frac{\mathbf{C}_b^n(t+\delta t)-\mathbf{C}_b^n(t)}{\delta t} \\ &= \lim_{\delta t\to 0}\frac{\mathbf{C}_b^n(t)(\mathbf{I}+\delta\boldsymbol{\Psi})-\mathbf{C}_b^n(t)}{\delta t} = \lim_{\delta t\to 0}\frac{\mathbf{C}_b^n(t)\delta\boldsymbol{\Psi}}{\delta t} \\ &= \mathbf{C}_b^n(t)\lim_{\delta t\to 0}\frac{\delta\boldsymbol{\Psi}}{\delta t} = \mathbf{C}_b^n\boldsymbol{\Omega}_{nb}^b \end{aligned} \tag{2.25}$$

where

$$\boldsymbol{\Omega}_{nb}^b = \begin{bmatrix} 0 & -\omega_z & \omega_y \\ \omega_z & 0 & -\omega_x \\ -\omega_y & \omega_x & 0 \end{bmatrix} \tag{2.26}$$

2.1.2.3 Quaternion

The propagation of quaternion $\mathbf{q}_b^n$ follows the form of quaternion multiplication as bellow

$$\dot{\mathbf{q}}_b^n = \frac{1}{2}\mathbf{q}_b^n \cdot \mathbf{p}_{nb}^b \tag{2.27}$$

where $\mathbf{p}_{nb}^b = \begin{bmatrix} 0 & \boldsymbol{\omega}_{nb}^b \end{bmatrix}^{\mathrm{T}}$, and the quaternion multiplication can be transformed into matrix-vector multiplication as

$$\begin{bmatrix} \dot{q}_0 \\ \dot{q}_1 \\ \dot{q}_2 \\ \dot{q}_3 \end{bmatrix} = \frac{1}{2}\begin{bmatrix} q_0 & -q_1 & -q_2 & -q_3 \\ q_1 & q_0 & -q_3 & q_2 \\ q_2 & q_3 & q_0 & -q_1 \\ q_3 & -q_2 & q_1 & q_0 \end{bmatrix}\begin{bmatrix} 0 \\ \omega_x \\ \omega_y \\ \omega_z \end{bmatrix} = \frac{1}{2}\mathbf{W}\mathbf{q} \tag{2.28}$$

where

$$\mathbf{W} = \begin{bmatrix} 0 & -\omega_x & -\omega_y & -\omega_z \\ \omega_x & 0 & \omega_z & -\omega_y \\ \omega_y & -\omega_z & 0 & \omega_x \\ \omega_z & \omega_y & -\omega_x & 0 \end{bmatrix} \tag{2.29}$$

The discretized solution of Eq. (2.28) may be written as

$$\mathbf{q}_{k+1} = \left[\exp \frac{1}{2}\int_{t_k}^{t_{k+1}} \mathbf{W} dt \right] \mathbf{q}_k \tag{2.30}$$

By reorganizing Eq. (2.30), the matrix-vector multiplication can be transformed into quaternion multiplication as

$$\mathbf{q}_{k+1} = \mathbf{q}_k \cdot \mathbf{r}_k \tag{2.31}$$

where

$$\mathbf{r}_k = \begin{bmatrix} a_c & a_s\sigma_x & a_s\sigma_y & a_s\sigma_z \end{bmatrix}^{\mathrm{T}}, \tag{2.32}$$

$$\sigma_x = \omega_x dt\,,\ \ \sigma_y = \omega_y dt\,,\ \ \sigma_z = \omega_z dt\,, \tag{2.33}$$

$$a_c = \cos\left(\frac{\sigma}{2}\right), a_s = \sin\left(\frac{\sigma}{2}\right), \tag{2.34}$$

and

$$(0.5\sigma)^2 = 0.25(\sigma_x^2 + \sigma_y^2 + \sigma_z^2)\,. \tag{2.35}$$

In this thesis, quaternion update is selected for navigation simulation.

2.1.3 Velocity and position update algorithm

In the local geographic navigation frame, the velocity update can be performed by Eq. (2.12). The turning rate of earth rotation and the transport rate expressed in the local geographic frame are written as follows with the consideration of the shape of the Earth:

$$\boldsymbol{\omega}_{ie}^{n} = \begin{bmatrix} \omega_{ie}\cos L & 0 & -\omega_{ie}\sin L \end{bmatrix}^{T} \tag{2.36}$$

$$\boldsymbol{\omega}_{en}^{n} = \begin{bmatrix} \dfrac{v_E}{R_E + h} & \dfrac{-v_N}{R_N + h} & \dfrac{-v_E \tan L}{R_E + h} \end{bmatrix} \tag{2.37}$$

where

$$R_N = \frac{R(1-e^2)}{(1-e^2\sin^2 L)^{3/2}}\,, \tag{2.38}$$

$$R_E = \frac{R}{(1-e^2 \sin^2 L)^{1/2}}, \tag{2.39}$$

$$f = (R-r)/R, \tag{2.40}$$

$$e = \left[f\left(2-f\right)\right]^{1/2}, \tag{2.41}$$

R is length of the semi-major axis, r is length of the semi-minor axis, f is the flattening of the ellipsoid, e is major eccentricity of the ellipsoid, h is height of the vehicle, L is the latitude, v_N and v_E are velocity of the north and east direction, respectively. R_N is the radius of the ellipsoid when the Earth is cut by the surface that is spanned by the north and down axis of the local geographic navigation frame. In the similar way, R_E is the radius of the ellipsoid generated as the Earth is cut by the surface that is spanned by the east and down axis of the local geographic navigation frame. R_N and R_E is often called as a meridian radius of curvature (R_m) and a transverse radius of curvature (R_t) respectively.

The change rate of the latitude, longitude and height are written as

$$\dot{L} = \frac{v_N}{R_N + h} \tag{2.42}$$

$$\dot{l} = \frac{v_E}{\left(R_E + h\right)\cos L} \tag{2.43}$$

$$\dot{h} = -v_D \tag{2.44}$$

The overall INS process is shown in Figure 2.2

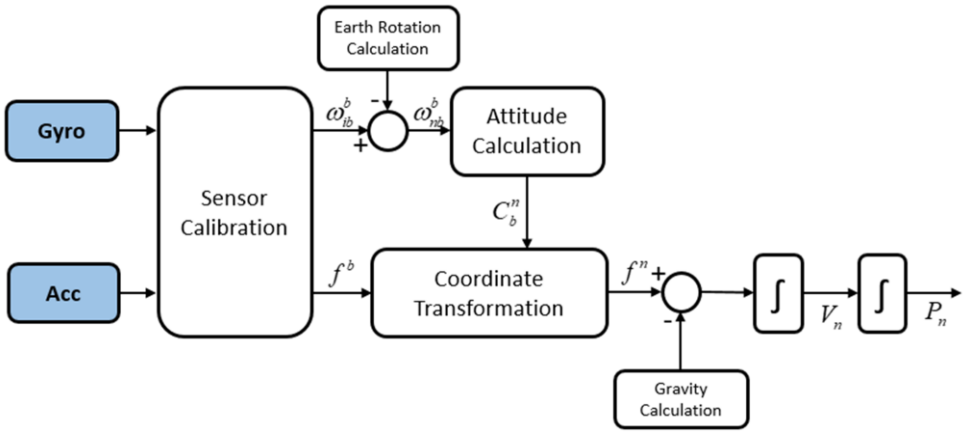

Figure 2.2: Overall INS process

2.2 Redundant inertial measurement units (RIMU)

Inertial navigation of RIMU is not so different from that of conventional IMU but the acceleration and gyro outputs are estimated from redundant sensors. Since the RIMU has advantage in redundancy, the fault detection and isolation (FDI) algorithm is also available, promising the reliability for the long term navigation. However, the problem is that the performance of navigation and FDI are both affected by the orientation of the sensing axes. Therefore, in this part, the configuration of the sensing axes orientation is mainly reviewed in terms of the optimal navigation and FDI performance.

2.2.1 Sensing axes configuration for optimal navigation performance

Suppose that there is a RIMU with *n*-axes accelerometers/gyroscopes. Then, the inertial measurement sensed in *n*th sensors can be depicted as Figure 2.3. The measurement equations of *n* sensors can be written as

$$\begin{bmatrix} m_1 \\ m_2 \\ \vdots \\ m_n \end{bmatrix} = \begin{bmatrix} \mathbf{i}\cdot\mathbf{S}^1 & \mathbf{j}\cdot\mathbf{S}^1 & \mathbf{k}\cdot\mathbf{S}^1 \\ \mathbf{i}\cdot\mathbf{S}^2 & \mathbf{j}\cdot\mathbf{S}^2 & \mathbf{k}\cdot\mathbf{S}^2 \\ \vdots & \vdots & \vdots \\ \mathbf{i}\cdot\mathbf{S}^n & \mathbf{j}\cdot\mathbf{S}^n & \mathbf{k}\cdot\mathbf{S}^n \end{bmatrix} \begin{bmatrix} w_x \\ w_y \\ w_z \end{bmatrix} + \begin{bmatrix} n_1 \\ n_2 \\ \vdots \\ n_n \end{bmatrix} \tag{2.45}$$

which can be summarized as

$$\mathbf{z}(k) = \mathbf{H}\mathbf{x}(k) + \mathbf{n}(k) \tag{2.46}$$

where $\mathbf{z}(k)$ is a $n \times 1$ vector composed of measurements from *n* sensors, $\mathbf{H}$ is a Jacobian matrix, w_x, w_y, and w_z is linear accelerations or angular velocity resolved in body frame, and $\mathbf{n}(k)$ is a $n \times 1$ vector composed of noise included

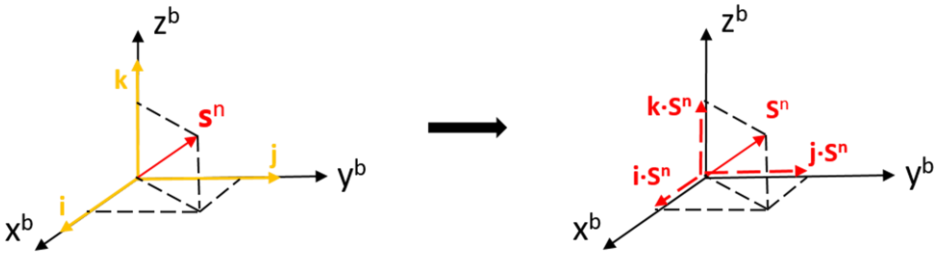

Figure 2.3: Inertial measurement sensed in the *n*th sensor

in sensors. It is assumed that each sensor has ideally calibrated. Then, the estimated solution can be derived as

$$\hat{\mathbf{x}} = (\mathbf{H}^T\mathbf{H})^{-1}\mathbf{H}^T\mathbf{z} \tag{2.47}$$

which is the result of conventional least squares. If estimation error is defined as

$$\mathbf{e} = \mathbf{x} - \hat{\mathbf{x}} \tag{2.48}$$

The covariance of estimation error $\mathbf{P}_e$ can be derived as

$$\mathbf{P}_\mathbf{e} = E[\mathbf{e}\mathbf{e}^T] = \sigma^2(\mathbf{H}^T\mathbf{H})^{-1} = \sigma^2\mathbf{P} \tag{2.49}$$

where σ indicates the noise level of sensing axes. In this case, all sensors show identical level of noise.

The cost function for minimizing estimation error can be set base on the characteristic of $\mathbf{P}$, which is explained in Table 2.1. Typically, the cost function is called as a figure of merit (FOM). Although the cost function is different in terms of the sensitivity of the change rate in function value, the mathematical meanings are all identical, which is related to minimizing estimation error.

Eventually, the criteria for optimizing navigation performance can be summarized as

$$\arg\min_{\mathbf{P}}(\mathrm{FOM}1,2,3) = \left(\mathbf{H}^T\mathbf{H}\right)^{-1} = \frac{3}{n}\mathbf{I} \tag{2.50}$$

where *n* is the number of sensors used. The various configuration of RIMU is listed through Figure 2.4 to Figure 2.8 according to the various number of the inertial sensors[8].

Table 2.1: List of FOM and its meaning

FOM	Mathematical meaning
$\mathrm{Tr}(\mathbf{P})$	Geometric dilution of precision
$\sqrt{\det(\mathbf{P})}$	Volume of error ellipsoid
$\lambda_{\max}(\mathbf{P})$	Worst case estimation error (maximum eigenvalue of error covariance matrix)

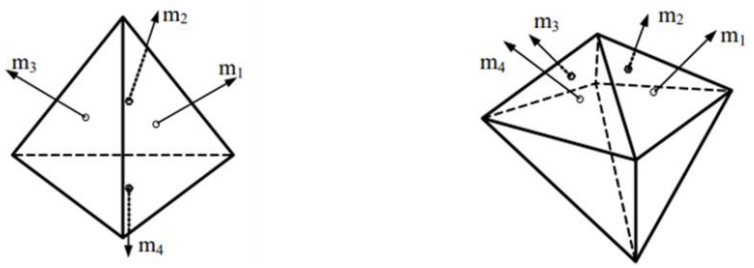

(a) Tetrahedron (b) Octahedron

Figure 2.4: Configuration of sensor orientation for optimal navigation performance with 4 sensing axes

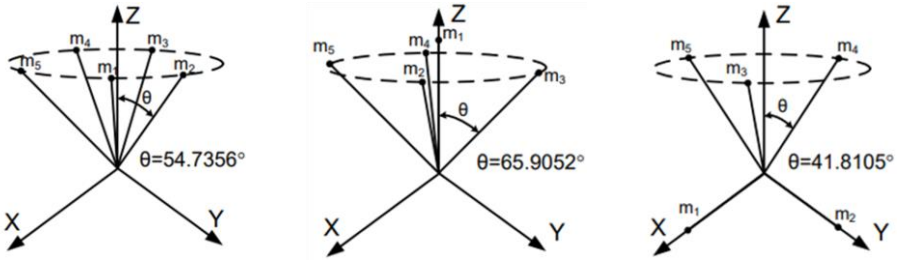

(a) Cone-type (b) Cone-type with a sensor on z-axis (c) Cone-type with a sensor on x, y-axis each

Figure 2.5: Configuration of sensor orientation for optimal navigation performance with 5 sensing axes

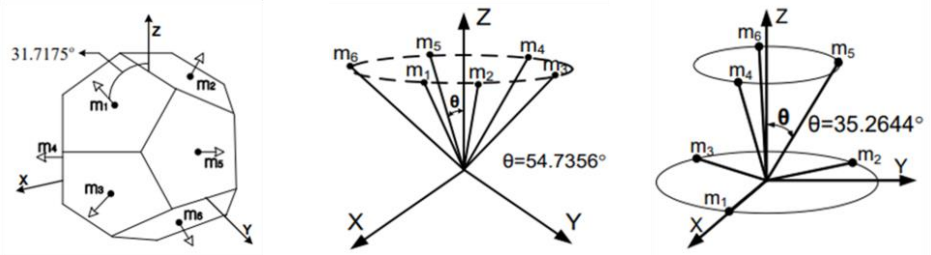

(a) Dodecahedron (b) Cone-type (c) Cone-type with sensors on x-y plane

Figure 2.6: Configuration of sensor orientation for optimal navigation performance with 6 sensing axes

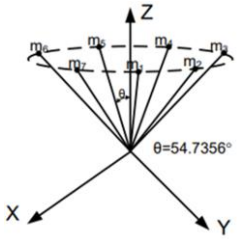

(a) Cone-type

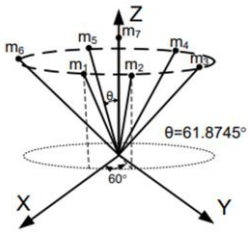

(b) Cone-type with a sensor on z-axis

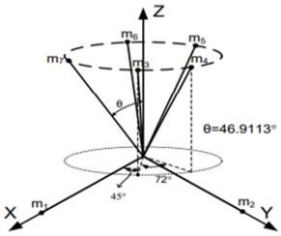

(c) Cone-type with sensors on x-y plane

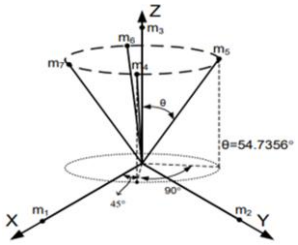

(d) Cone-type with sensors on each axis

Figure 2.7: Configuration of sensor orientation for optimal navigation performance with 7 sensing axes

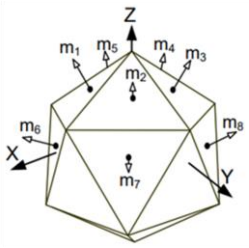

(a) Icosahedron 1

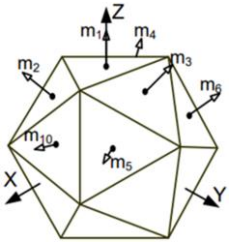

(b) Icosahedron 2

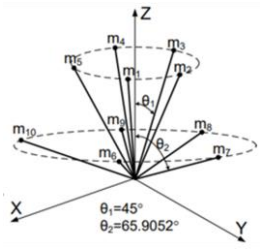

(c) Double cone-type

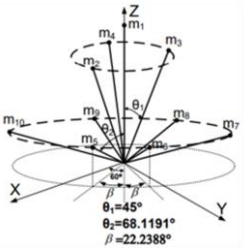

(d) Double cone-type with a sensor on z-axis

Figure 2.8: Configuration of sensor orientation for optimal navigation performance with 10 sensing axes

2.2.2 Sensing axes configuration for optimal FDI performance

The FDI algorithm may be derived from setting parity equations using Jacobian matrix in Eq. (2.51). Let v_i be an n-dimensional vector that satisfies:

$$\mathbf{v}_i^{\mathrm{T}}\mathbf{H} = 0 \tag{2.51}$$

Although v_i may be an arbitrary vector, the matrix $\mathbf{V}$, which is constructed by v_i, shows rank of at most n-3[33]. Therefore, the minimum number required for isolating sensor faults is derived as 5. The choice of $\mathbf{V}$ can be performed based on the following two constraints:

$$\mathbf{VH} = 0 \tag{2.52}$$

$$\mathbf{VV}^{\mathrm{T}} = \mathbf{I} \tag{2.53}$$

where Gram Schmidt orthogonalization can be considered to resolve $\mathbf{V}$.

Finally, the parity equations can be constructed as

$$\mathbf{p} = \mathbf{Vz} \tag{2.54}$$

where $\mathbf{z}$ is the measurement vector from Eq. (2.46). Base on the parity equations, the decision function for fault detection (DF_D) and fault isolation ($DF_{I,j}$) may be defined as

$$DF_D = \mathbf{p}^T\mathbf{p} \tag{2.55}$$

$$DF_{I,j} = (\mathbf{p}^T\mathbf{v}_j)^2 \tag{2.56}$$

where DF_D is compared with the properly adjusted threshold so that if its value

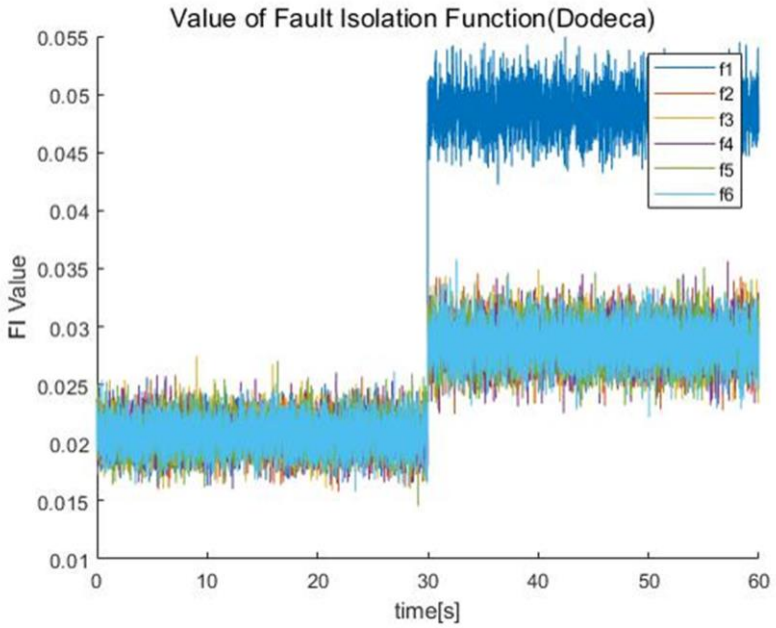

Figure 2.9: Change of decision value function related to fault isolation

is over the threshold, the algorithm gives fault alarm. If fault alarms operates, $DF_{I,j}$ is calculated through all redundant sensors, where j is the index for the sensors. Then, the index number for the maximum value of $DF_{I,j}$ can be regarded as a faulty sensor. The example of FDI operation is described in Figure 2.9, where the RIMU of dodecahedron configuration, consists of 6-sensing axes, have fault measurements on sensor #1 at 30s.

By adding specific constraint on the FOM, the configuration of sensing axes for the optimal FDI performance can be selected from the configurations listed in 2.1.1 The revised form of cost function is as bellow.

$$J = \max_{i,j(i<j)} \left| \mathbf{h}_i \mathbf{h}_j^T \right| \text{ subject to } \left(\mathbf{H}^T \mathbf{H} \right)^{-1} = \frac{3}{n} \mathbf{I} \tag{2.57}$$

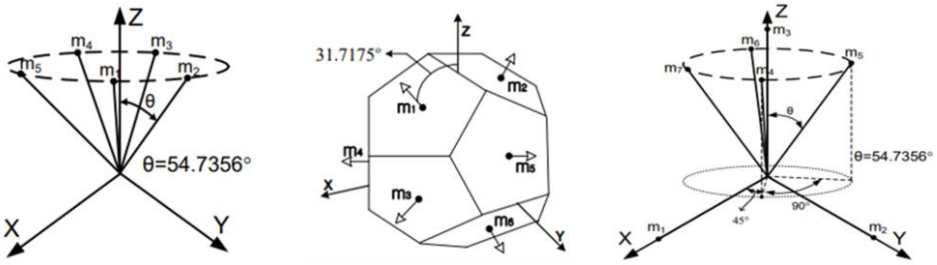

(a) Cone-type (b) Dodecahedron (c) Cone-type with sensors on x-y plane

Figure 2.11: Configuration of sensor orientation for optimal FDI performance with 5, 6, and 7 sensing axes

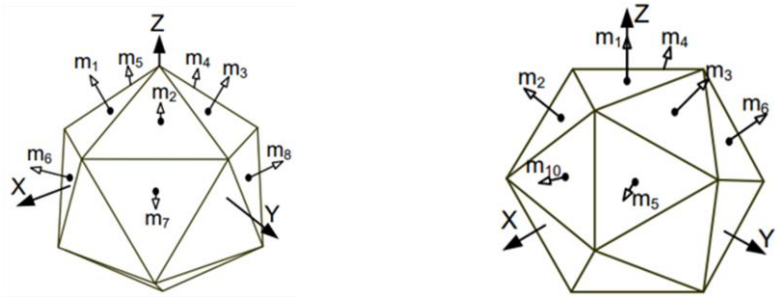

(a) Icosahedron 1 (b) Icosahedron 2

Figure 2.10: Configuration of sensor orientation for optimal FDI performance with 10 sensing axes

Eq. (2.57) means picking the configurations that has maximum angle between the neighboring sensing axes. The configuration that shows maximum J among previously proposed configurations are listed in Figure 2.11 and Figure 2.10.

Chapter 3

Inertial Navigation based on RIMU

In this chapter, the analysis on the navigation performance based on the RIMU outputs are performed. Intuitively, it is natural that the navigation performance improves with the measurements from redundant sensors where more information is used to estimate linear acceleration or angular velocity of body frame. Given that all the redundant sensors are ideally calibrated, the exact value of decrement in noise level can be derived, which leads to the navigation performance enhancement.

However, the size of the inertial sensors cannot be neglected, which induces the unwanted extra specific force such as Euler force and centrifugal force added to the measurements of acceleration when angular motions are applied. The measurement error in this case can be named as the lever arm effect, because the unexpected specific force is induced from the lever arm in real world RIMU case.

Conventionally, this effect has been minimized by optimizing lever arm vectors along the redundant sensors, assigning optimized length to the lever arm of each of the inertial sensors. The suppressing effect of this methodology is reviewed through simulation, and the limitations are specified, which highlight the need for improved methods.

3.1 Navigation performance analysis

3.1.1 Performance enhancement according to the number of redundant sensors

Substituting Eq. (2.50) into Eq. (2.49) leads to:

$$\mathbf{P}_{\mathbf{e}} = E[\mathbf{e}\mathbf{e}^T] = \sigma^2(\mathbf{H}^T\mathbf{H})^{-1} = \sigma^2 \frac{3}{n}\mathbf{I} \tag{3.1}$$

which implies that the noise level of RIMU is reduced with the factor of $\sqrt{3/n}$. This can be confirmed in Figure 3.1.

The navigation error induced by sensor noise cannot be resolved in deterministic manner. Therefore, the navigation performance according to the number of sensing axes is analyzed by Monte Carlo simulation. The sensor noise

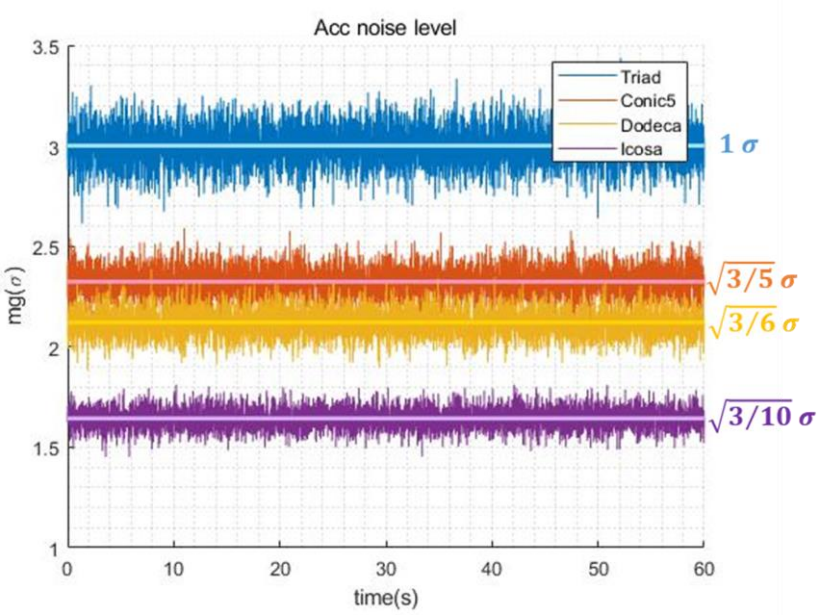

Figure 3.1: Noise level reduction according to the number or redundant sensors

specification used in the simulation is $300ug/\sqrt{Hz}$, $0.1deg/hr/\sqrt{Hz}$ respectively for accelerometer and gyroscope, and the sampling rate is $100Hz$. The configurations used are listed in Figure 3.2. The vehicle used in simulation runs along the straight line for 60 seconds in order to exclude the lever arm effect. Improvement of navigation performance with the additional number of redundant sensors can be confirmed in Figure 3.3

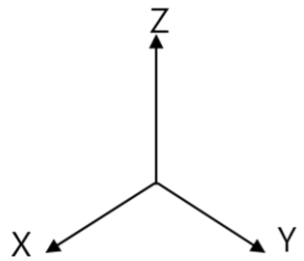

(a) Orthogonal 3 sensing axes

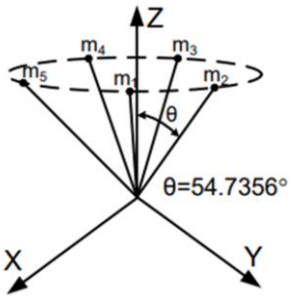

(b) Cone-type (5 sensing axes)

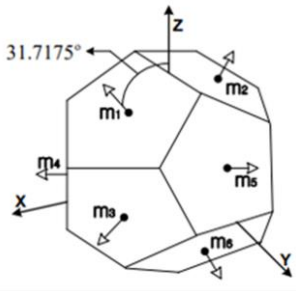

(c) Dodecahedron

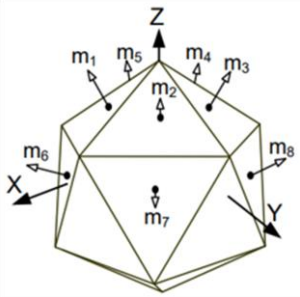

(d) Icosahedron

Figure 3.2: Configuration used for navigation simulation

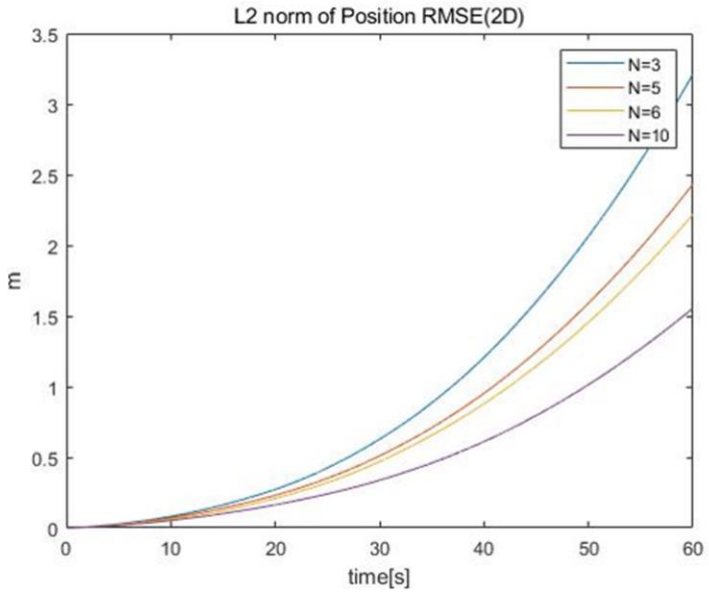

Figure 3.3: Position RMSE with various number of redundant sensors

3.1.2 Performance degradation due to the presence of the lever arm

The lever arm effect can be confirmed in the following equation as

$$f_i = \mathbf{h}_i \cdot \left\{ \mathbf{f} + \dot{\boldsymbol{\omega}} \times \mathbf{d}_i + \boldsymbol{\omega} \times \left(\boldsymbol{\omega} \times \mathbf{d}_i \right) \right\} \tag{3.2}$$

where $\mathbf{d}_i$ is a lever arm vector for each of the redundant sensor. In order to reduce the navigation error induced by lever arm effect, the latter two terms, which is $\dot{\boldsymbol{\omega}} \times \mathbf{d}_i$ and $\boldsymbol{\omega} \times \left(\boldsymbol{\omega} \times \mathbf{d}_i \right)$ where each of it stands for the Euler force and centrifugal force respectively, should be compensated.

The Euler force is typically excluded by aligning the orientation of sensing axes and its corresponding lever arm vector, since the noise level of angular acceleration is inevitably bigger than that of angular rate. Also, thanks to the fact

that the measurement of angular rate is not affected by lever arm effect, which is

$$\omega_i = \mathbf{h}_i \cdot \boldsymbol{\omega}, \tag{3.3}$$

the estimation of angular rate is performed firstly in order to compensate the centrifugal force in Eq. (3.2). Although the estimates of the angular rate include some noise, for the IMUs with higher specification including tactical grade or navigation grade, the noise level of gyroscopes has little effect on the estimation.

To examine the effect of the lever arm on navigation performance, maximum turning rate about $180\,\mathrm{deg/sec}$ at x, y, and z axis of body frame is applied. The turning motion is described in Figure 3.4, where there are 2.5 seconds of static segments which is included to visualize the lever arm effect. To configure the orientation of sensing axes in RIMU, the tetrahedron in Figure 2.4 is used. The

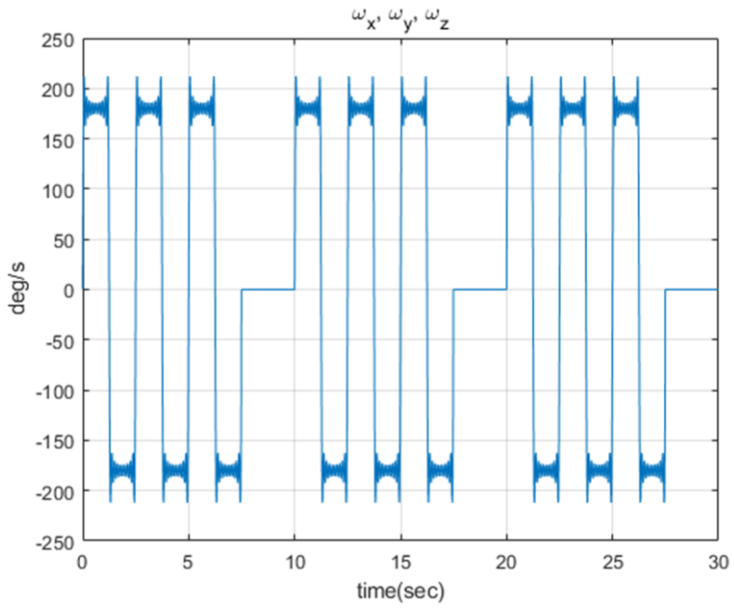

Figure 3.4: Turning motion of given RIMU configuration

noise level of the accelerometer and gyroscopes that comprises RIMU is set to be $190\,ug/\sqrt{Hz}$ and $0.1\,deg/hr/\sqrt{Hz}$.

According to the Figure 3.5, it seems that there is no problem in estimating acceleration with low noise of gyroscopes. However, the remaining estimation error can be visualized with the low cost gyroscopes. if the gyroscope has noise level of $72\,deg/hr/\sqrt{Hz}$, the results of acceleration estimation including typical compensating method can be inspected in Figure 3.6.

As RIMU usually use low cost mems IMU for its component rather than a tactical grade or navigation grade, the necessity to remove the lever arm effect

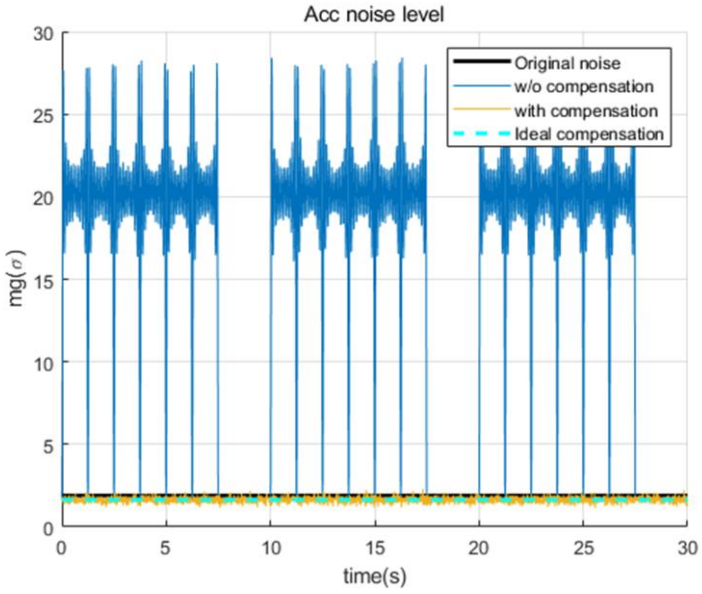

Figure 3.5: Acceleration estimates with/without lever arm effect compensation (lower gyroscope noise)

cannot be neglected.

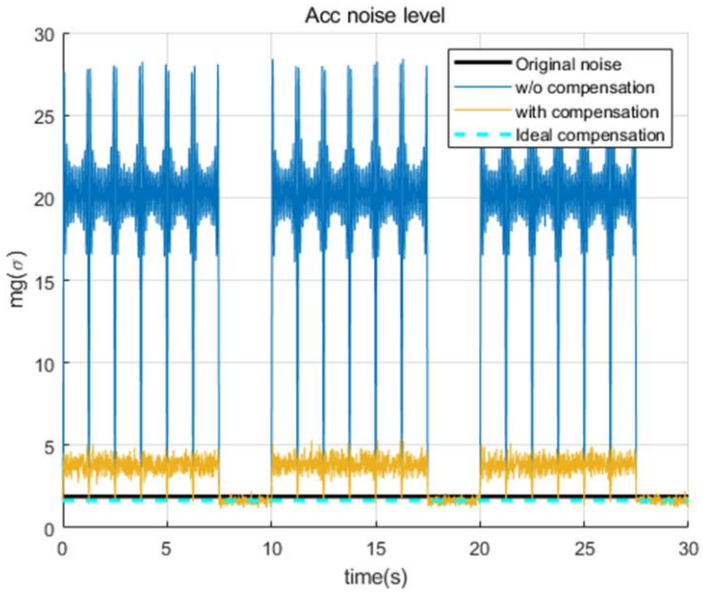

Figure 3.6: Acceleration estimates with/without lever arm effect compensation (higher gyroscope noise)

3.1.3 Lever arm optimization for minimizing the lever arm effect

One of the proposed method to minimize the lever arm effect is to solve the optimization problem regarding the length of the lever arm with the assumption that physical shape of each inertial sensor is approximated as a sphere of radius r [6]. The overall process is derived as bellows.

If each lever arm vectors are aligned with the orientation of the belonging sensing axes, the following is satisfied:

$$\mathbf{h}_i \cdot \left(\dot{\boldsymbol{\omega}} \times \mathbf{d}_i \right) = \left(\mathbf{d}_i \times \mathbf{h}_i \right)^{\mathrm{T}} \dot{\boldsymbol{\omega}} = 0 \tag{3.4}$$

which means that Euler forces measured in each sensors are excluded mathematically. By assuming that center of gravity of the redundant sensor assembly is equal to the origin of the case frame, the sum of all lever arm vectors

can be written as

$$\sum_{i=1}^{n} \mathbf{d}_i = \sum_{i=1}^{n} k_i \mathbf{h}_i = 0 \tag{3.5}$$

where k_i is the coefficient for the lever arm vectors. Eq. (3.5) can be reformulated by using matrix and vector notation as

$$\begin{bmatrix} \mathbf{h}_1 & \mathbf{h}_2 & \cdots & \mathbf{h}_n \end{bmatrix} \begin{bmatrix} k_1 \\ k_2 \\ \vdots \\ k_n \end{bmatrix} = \mathbf{H}^{\mathrm{T}} \mathbf{k} = 0 \tag{3.6}$$

Using Eq. (3.6) as an additional constraint, the optimal $\mathbf{k}$ can be selected by solving the following equation:

$$\mathbf{k}_{optimal} = \underset{\mathbf{k}, |k_i \mathbf{h}_i - k_j \mathbf{h}_j| \geq 2r}{\arg\min} \left\| \mathbf{k} \right\|_{\infty} \tag{3.7}$$

which subjects to Eq. (2.50) and Eq. (3.6), where r is a radius for sphere to which each sensors physical shape is approximated.

For a conic configuration with 4 redundant sensors, the Jacobian matrix of measurement equation is given as follows:

$$\mathbf{H} = \begin{bmatrix} \sin\alpha & 0 & \cos\alpha \\ 0 & \sin\alpha & \cos\alpha \\ -\sin\alpha & 0 & \cos\alpha \\ 0 & -\sin\alpha & \cos\alpha \end{bmatrix} \tag{3.8}$$

where $\alpha = 54.7356^{\circ}$, and its optimized lever arm may be calculated as

$$\mathbf{k}_{optimal} = \left[\frac{r}{\sin\alpha} \quad -\frac{r}{\sin\alpha} \quad \frac{r}{\sin\alpha} \quad -\frac{r}{\sin\alpha} \right]^{\mathrm{T}} \tag{3.9}$$

For a conic configuration with 5 redundant sensors, the Jacobian matrix of measurement equation is given as follows:

$$\mathbf{H} = \begin{bmatrix} \sin\alpha & 0 & \cos\alpha \\ 0 & \sin\alpha & \cos\alpha \\ -\sin\alpha & 0 & \cos\alpha \\ 0 & -\sin\alpha & \cos\alpha \\ 0 & 0 & -1 \end{bmatrix} \tag{3.10}$$

where $\alpha = 65.9052^{\circ}$, and its suboptimal length of the lever arm can be calculated as

$$\mathbf{k}_{optimal} = \begin{bmatrix} 2r & -2r & 2r & -2r & 0 \end{bmatrix}^{\mathrm{T}} \tag{3.11}$$

Also, the results of lever arm optimization is visualized in Figure 3.8 and Figure 3.7.

For the lever arm vectors derived in an optimized manner, the lever arm effect can be compensated in Eq. (3.2), which leads to the minimization in estimation error of linear acceleration.

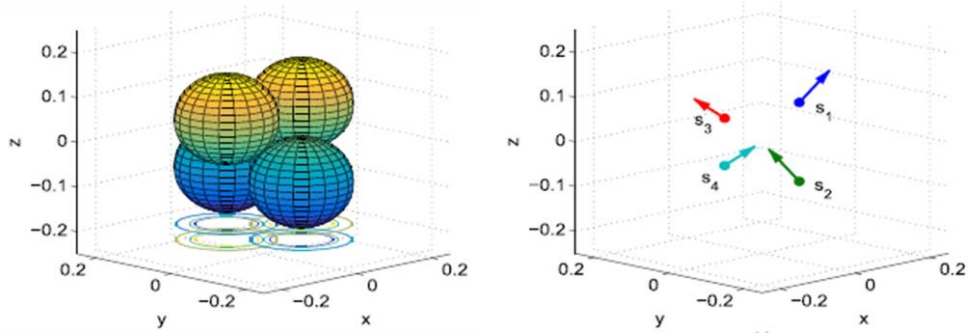

(a) Sensing axes orientation (b) Lever arm configuration

Figure 3.8: Optimized lever arm vector with 4 sensing axes[6]

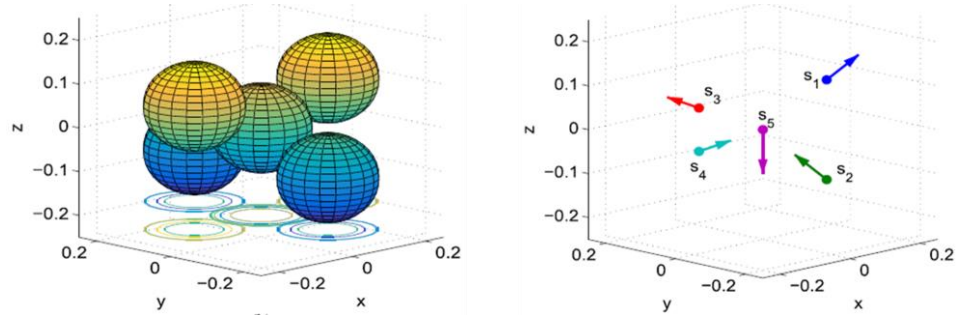

(a) Sensing axes orientation (b) Lever arm configuration

Figure 3.7: Optimized lever arm vector with 5 sensing axes[6]

Chapter 4

Mitigating Lever Arm Effect in RIMU

In the previous chapter, the effect of lever arm is minimized by assigning optimal length to each lever arm vectors that are aligned with direction of sensing axes. However, estimation error still remains when applying least squares with compensated measurements. Also, the optimal configuration of the lever arm vectors should be calculated whenever the Jacobian matrix change, which is cumbersome as the number of redundant sensors increases. The method suggested in 3.1.3 also assume the shape of each sensors as a sphere, which means that the result of the solution is shape-dependent.

To solve the listed above, two methods to remove the lever arm effect in RIMU is suggested in this chapter. These methods include the configuration of the lever arm vectors in an easier way with a suitable measurement fusion method. The performance of the suggested algorithms is shown by simulation.

4.1 Symmetric lever arm configuration based on least squares method

4.1.1 Lever arm configuration

Suppose a RIMU which has its origin at point P and composed of two identical subsets. From now on, each of the subset will be called as a “basis

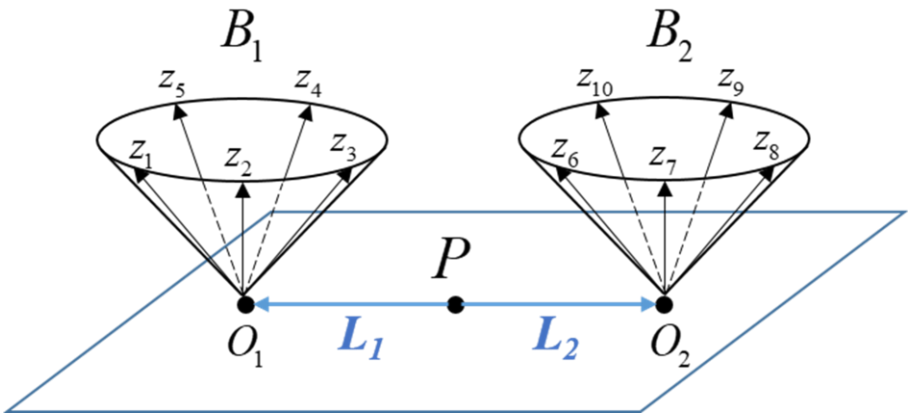

Figure 4.1: Double conic configuration with symmetric lever arm vector

configuration." Figure 4.1 is the RIMU composed of basis configuration B_1 and B_2, where O_1 and O_2, is their own origin. Any kind of previously proposed configuration (platonic solids, cone, etc.) can be set to form a basis configuration for the optimal navigation performance. However, for the simplicity of visualization, the conical shape with the zero-length lever arm ($\mathbf{d}_i = 0$) is chosen.

Define the lever arm vector $\mathbf{L}_1$ starting from P and ends at O_1. If O_2 is placed where O_1 is mirrored with respect to point P, the lever arm vector $\mathbf{L}_2$ has the same magnitude as $\mathbf{L}_1$ but the opposite direction (namely, $\mathbf{L}_1 = -\mathbf{L}_2$). For the case when a basis configuration B_1 has its own non-zero lever arm vectors $\mathbf{d}_i$ ($i = 1, \cdots, 5$) starting from their origin O_1, the corresponding counterpart B_2 should have their lever arm vectors $\mathbf{d}_j$ ($j = 1, \cdots, 5$) so that $\mathbf{L}_1 + \mathbf{d}_i = -(\mathbf{L}_2 + \mathbf{d}_j)$.

With the careful inspection of Eq. (3.2), the two latter terms related to angular rate $\boldsymbol{\omega}$ and angular acceleration $\dot{\boldsymbol{\omega}}$ are both multiplied once by the lever arm vector $\mathbf{d}_i$. Therefore, Euler force and centrifugal force measured by the sensor

axis $z_1 \sim z_5$ of B_1 have the exact same magnitude but the opposite direction at $z_6 \sim z_{10}$ of B_2. Eventually, the lever arm effect can be offset by each other, and the LS does not suffer from estimation error by the unwanted lever arm related force. The exact proof is shown in part III.

By placing multiple pairs of basis configuration which have the exactly symmetric lever arm around the point P, the number of sensing axes can be safely added without suffering from the lever arm effect. Note that no process of optimization related to the lever arm vector is required for this kind of approach.

4.1.2 Measurement fusion

The followings are the process of proof that the sum of nonlinear equations based on each basis configuration can be transformed into a single linear equation without loss of generality. Suppose that there are *m* pairs of basis configurations, where each configuration is composed of *n* sensing axes (For example, RIMU configuration of Figure 4.1 is the case for $m=1$, and $n=5$). In Figure 4.2, the

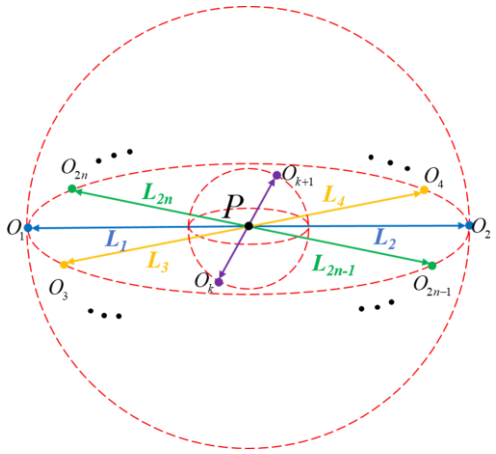

Figure 4.2: General expression of lever arm configuration of RIMU with symmetric lever arm assignment

possible origins of each basis configuration are distributed around the RIMU case origin P, and each of the symmetric counterpart is depicted as the same color, where $\mathbf{L}_i + \mathbf{d}_i = -(\mathbf{L}_{i+1} + \mathbf{d}_{i+1})$ for all $i = 1, 3, \cdots, 2n-1$. Note that different pairs of configurations may have different lengths of lever arm compared to other pairs, which means that several layers of the spherical formulation of the different radius can be added. For example, O_k and O_{k+1} are the points on the smaller sphere in Figure 4.2.

The measurement equation related to linear acceleration of basis configuration centered on O_1 in Figure 4.2 can be expressed as

$$\begin{bmatrix} f_1 \\ \vdots \\ f_n \end{bmatrix} = \begin{bmatrix} \mathbf{h}_1^{\mathrm{T}} \\ \vdots \\ \mathbf{h}_n^{\mathrm{T}} \end{bmatrix} \mathbf{f} + \begin{bmatrix} \mathbf{h}_1^{\mathrm{T}} \left(\dot{\boldsymbol{\omega}} \times \left(\mathbf{L}_1 + \mathbf{d}_1 \right) \right) + \mathbf{h}_1^{\mathrm{T}} \boldsymbol{\Omega}^2 \left(\mathbf{L}_1 + \mathbf{d}_1 \right) \\ \vdots \\ \mathbf{h}_n^{\mathrm{T}} \left(\dot{\boldsymbol{\omega}} \times \left(\mathbf{L}_1 + \mathbf{d}_n \right) \right) + \mathbf{h}_n^{\mathrm{T}} \boldsymbol{\Omega}^2 \left(\mathbf{L}_1 + \mathbf{d}_n \right) \end{bmatrix} + \mathbf{v} \qquad (4.1)$$

Note that the noise level of angular acceleration would be inevitably greater than the angular rate, and its value would be amplified by the sampling rate. Considering the effect of the misalignment in each sensor, it is better to align the lever arm vectors to its corresponding sensing axes in order to cancel out the Euler force by using symmetric lever arm configuration. Therefore, the additional constraints of the lever arm vectors should be $\mathbf{L}_j + \mathbf{d}_i \,||\, \mathbf{h}_i$ for all $i = 1, 2, \cdots, 2n$ and $j = 1, 2, \cdots, m$, where the length of the vector $\mathbf{L}_j$ should be 0cm to satisfy the constraints.

An example of basis configuration and its total configuration when $m = 1$, $n = 5$, $L = 0cm$, $d = 1cm$ is shown in Figure 4.3. In this case, there are ten sensing axes, composed of conical shaped basis configuration of 5 sensing axes.

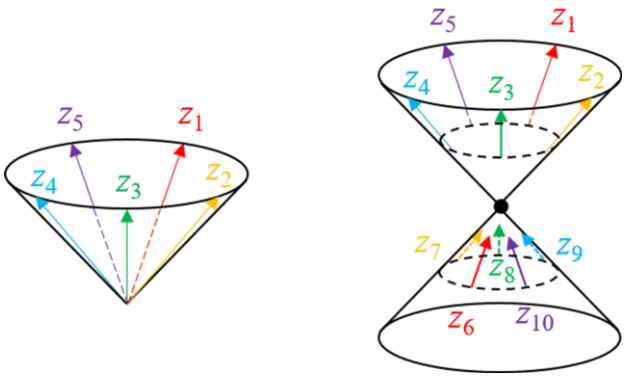

Figure 4.3: RIMU composed of a pair of conic configuration with 10 sensing axes

And every length of the lever arm from the center of RIMU is $L + d = 1cm$.

If the term regarding the lever arm effect is denoted as $\mathbf{L}^i$, where i is the index for a pair of basis configuration, the $2m$ measurement equations can be shown as

$$\begin{aligned} \mathbf{z}_{n\times 1}^1 &= \mathbf{H}\mathbf{x} + \mathbf{L}^1 + \mathbf{v}^1 \\ \mathbf{z}_{n\times 1}^2 &= \mathbf{H}\mathbf{x} - \mathbf{L}^1 + \mathbf{v}^2 \\ &\vdots \\ \mathbf{z}_{n\times 1}^{2m-1} &= \mathbf{H}\mathbf{x} + \mathbf{L}^m + \mathbf{v}^{2m-1} \\ \mathbf{z}_{n\times 1}^{2m} &= \mathbf{H}\mathbf{x} - \mathbf{L}^m + \mathbf{v}^{2m} \end{aligned} \tag{4.2}$$

where $\mathbf{z}_{n\times 1}^i$ represents the n measurements of acceleration, and $\mathbf{v}^i$ is the noise vector of the ith basis configuration. $\mathbf{x}$ is linear acceleration to be estimated, and $\mathbf{H}$ is the Jacobian matrix composed of sensing orientation vector $\mathbf{h}$.

If the noise vector in Eq. (4.2) follows Gaussian distribution with a mean of zero, the sum of $2m$ equations falls into

$$\frac{\mathbf{z}_{n\times 1}^1 + \mathbf{z}_{n\times 1}^2 + \cdots \mathbf{z}_{n\times 1}^{2n}}{2m} = \mathbf{H}\mathbf{x} + \mathbf{v}' \tag{4.3}$$

The total sum of the noise vector $\mathbf{v}'$ also follows Gaussian distribution because it is the sum of independent random variables of Gaussian distribution. Therefore, the summation of nonlinear equations eventually results in a single linear equation, where lever arm related term is eliminated as

$$\mathbf{z}' = \mathbf{H}\mathbf{x} + \mathbf{v}' \tag{4.4}$$

$$\mathbf{x}_{\mathrm{OLS}} = \left(\mathbf{H}^{\mathrm{T}}\mathbf{R}'^{-1}\mathbf{H}\right)^{-1}\mathbf{H}^{\mathrm{T}}\mathbf{R}'^{-1}\mathbf{z}' \tag{4.5}$$

where $\mathbf{R}' = \left(\mathbf{R}^1 + \mathbf{R}^2 + \cdots + \mathbf{R}^{2m}\right)/2m$, which represents the sum of $2n$ measurement covariance matrices divided by the total number of basis configuration. If the RIMU is composed of sensors with identical specification, then $\mathbf{R}' = \mathbf{R}$. Since the angular rate is not affected by the lever arm, the estimation is simply done by applying LS. As a result, the estimation of angular rate and linear acceleration is completed by conventional LS and Eq. (4.5), respectively.

4.1.3 Performance analysis

The Jacobian matrix in Eq. (4.4) using $2mn$ measurements is the same as the measurement equation using n sensors, but the difference in the estimation covariance can be demonstrated by the following procedure. Let $\mathbf{e}$ stands for the estimation error, which is the subtraction of estimates from the nominal value. Then,

$$\begin{aligned}\mathbf{e} &= \mathbf{x} - \hat{\mathbf{x}} = \mathbf{x} - \left(\mathbf{H}^T\mathbf{H}\right)^{-1}\mathbf{H}^T\left(\frac{\mathbf{z}_1 + \mathbf{z}_2 + \cdots + \mathbf{z}_{2m}}{2m}\right) \\ &= \mathbf{x} - \left(\mathbf{H}^T\mathbf{H}\right)^{-1}\mathbf{H}^T\left(\mathbf{H}\mathbf{x} + \frac{\mathbf{v}_1 + \mathbf{v}_2 + \cdots + \mathbf{v}_{2m}}{2m}\right) \\ &= -\left(\mathbf{H}^T\mathbf{H}\right)^{-1}\mathbf{H}^T\left(\frac{\mathbf{v}_1 + \mathbf{v}_2 + \cdots + \mathbf{v}_{2m}}{2m}\right)\end{aligned} \tag{4.6}$$

The covariance of $\mathbf{e}$ is defined as $\mathbf{P} = E\left[\mathbf{e}\mathbf{e}^{\mathrm{T}}\right]$, which is organized as

$$\begin{aligned}\mathbf{P} &= \frac{1}{4m^2}E\left[\left\{\left(\mathbf{H}^T\mathbf{H}\right)^{-1}\mathbf{H}^T\left(\mathbf{v}_1 + \cdots + \mathbf{v}_{2m}\right)\right\}\left\{\cdots\right\}^T\right] \\ &= \frac{2m\sigma^2}{4m^2}\mathbf{I}_{3\times 3}\left(\mathbf{H}^T\mathbf{H}\right)^{-1}\end{aligned} \tag{4.7}$$

By substituting Eq. (2.50) to Eq. (4.7),

$$\mathbf{P} = \frac{3}{2mn}\sigma^2\mathbf{I}_{3\times 3} \tag{4.8}$$

Therefore, the covariance of estimation is reduced as a factor of $3/2mn$, where $2mn$ is the total number of sensing axes.

4.2 Nonlinear least squares method

4.2.1 Lever arm configuration

The other way to determine the acceleration and angular rate from RIMU measurements is the estimation based on the nonlinear Eq. (3.2), which includes all the state variables including the angular acceleration. This kind of approach is widely applied in the research area such as biomechanics, which primarily focuses

on the motion-sensing of human body parts by gyro free (GF) IMUs. The GFIMUs are composed of multiple orthogonal accelerometers, where rotational motion herein is estimated using the Euler and centrifugal forces generated from relative motion between multiple sensors. There are some good literature to refer to, dealing with the principle of estimating rotational motion by GFIMUs [20]-[25].

One way to solve Eq. (3.2) with nonlinear least squares (NLS) is using the concentrated likelihood method, where the estimation process is divided into two stages. The theoretical proof of the concentrated likelihood method can be found on [26], and its application can be found on [27], where I. Skog applied this method in inertial array to estimate the extreme value of the angular rate where saturation of the gyroscope occurs.

At the first stage of the estimation, the turning rate is first to be determined with the weight of measurements is changed, namely, the likelihood is concentrated in order to maximize the likelihood for the afterward estimation. At the second stage, by substituting prior estimation of turning rate, Eq. (3.2) turns into a linear equation, including linear acceleration $\mathbf{f}$ and rotational acceleration $\dot{\boldsymbol{\omega}}$.

However, the naïve application of NLS aforementioned is not helpful for estimating triad solutions in the RIMU system. Since LS at the second stage includes both $\mathbf{f}$ and $\dot{\boldsymbol{\omega}}$, the estimation error of linear acceleration is affected by that of angular acceleration. In other words, as the number of state variables to be determined is increased with the same amount of measurements, the distribution of information occurs.

This problem can be solved by eliminating the angular acceleration term mathematically. Eq. (3.2) can be expressed with the multiplication of matrix and vector, which is described as Eq. (4.9). When the lever arm orientation is aligned

with the direction of the corresponding sensing axes, the value of $\left(\mathbf{d}_i \times \mathbf{h}_i\right)^{\mathrm{T}}$ goes to zero, eventually simplifying Eq. (3.2) to Eq. (4.10) with the removal of Euler force. Therefore, the necessity of estimating angular acceleration has disappeared, and the estimation of angular rate and linear acceleration is completed by applying NLS under measurement Eqs. (3.3) and (4.10).

$$\begin{aligned} f_i &= \mathbf{h}_i \cdot \mathbf{f} + \mathbf{h}_i \cdot \left(\dot{\boldsymbol{\omega}} \times \mathbf{d}_i\right) + \mathbf{h}_i \cdot \left[\boldsymbol{\omega} \times \left(\boldsymbol{\omega} \times \mathbf{d}_i\right)\right] \\ &= \mathbf{h}_i^{\mathrm{T}} \mathbf{f} + \left(\mathbf{d}_i \times \mathbf{h}_i\right)^{\mathrm{T}} \dot{\boldsymbol{\omega}}_i + \mathbf{h}_i^{\mathrm{T}} \boldsymbol{\Omega}^2 \mathbf{d}_i \end{aligned} \tag{4.9}$$

$$f_i = \mathbf{h}_i^{\mathrm{T}} \mathbf{f} + \mathbf{h}_i^{\mathrm{T}} \boldsymbol{\Omega}^2 \mathbf{d}_i \tag{4.10}$$

4.2.2 Measurement fusion

Suppose a RIMU composed of n accelerometers and n gyroscopes, each of them satisfying Eq. (2.50). Its configuration is described in Figure 4.4, where each of the accelerometer's sensing orientation is aligned with their lever arm

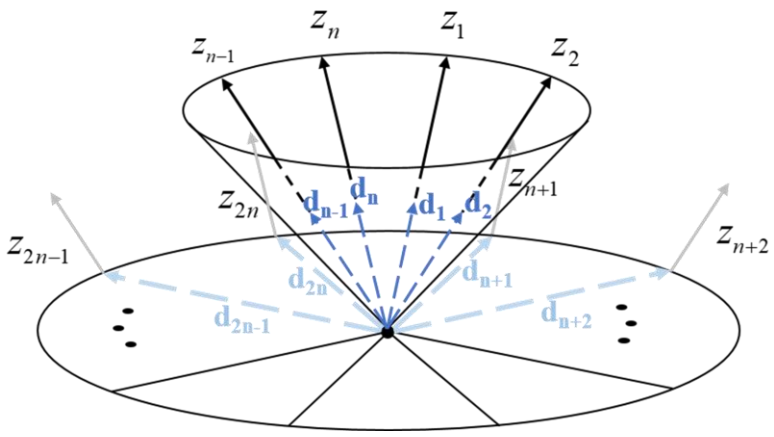

Figure 4.4: General expression of the lever arm configuration of RIMU with lever arms aligned with orientation of sensing axes

vectors, as mentioned in part II. To make the visualization simple and clear, the conic configuration is selected. $\mathbf{d}_i$ of $i=1,2,\cdots,n$ stands for the lever arm of ith accelerometer axis, and $\mathbf{d}_i$ of $i=n+1,n+2,\cdots,2n$ is the lever arm vector of gyroscopes. Note that as long as Eq. (2.50) is met, the placement of the gyroscopes' lever arm is not of interest. Nonlinear least squares based on the concentrated likelihood method is composed of two stages.

1) *Estimation of the angular rate*

The following measurement equation is a concatenate of Eqs. (3.3) and (4.10):

$$\begin{bmatrix} f_1 \\ \vdots \\ f_n \\ \omega_1 \\ \vdots \\ \omega_n \end{bmatrix} = \begin{bmatrix} \mathbf{h}_1^{\mathrm{T}}\boldsymbol{\Omega}_{\boldsymbol{\omega}}^2\mathbf{d}_1 \\ \vdots \\ \mathbf{h}_n^{\mathrm{T}}\boldsymbol{\Omega}_{\boldsymbol{\omega}}^2\mathbf{d}_n \\ \mathbf{h}_1^{\mathrm{T}}\boldsymbol{\omega} \\ \vdots \\ \mathbf{h}_n^{\mathrm{T}}\boldsymbol{\omega} \end{bmatrix} + \begin{bmatrix} \mathbf{h}_1^{\mathrm{T}} \\ \vdots \\ \mathbf{h}_n^{\mathrm{T}} \\ \mathbf{0}_{1\times 3} \\ \vdots \\ \mathbf{0}_{1\times 3} \end{bmatrix} \mathbf{f} + \begin{bmatrix} \mathbf{n}_f \\ \mathbf{n}_\omega \end{bmatrix} \tag{4.11}$$

which can be expressed as

$$\mathbf{z} = \mathbf{M}(\boldsymbol{\omega}, \mathbf{d}) + \mathbf{H}\mathbf{f} + \mathbf{n} \tag{4.12}$$

where $\mathbf{h}_i$ is the direction vector of the redundant sensors, $\mathbf{n}_f$ is a n dimensional vector composed of accelerometers' noise, $\mathbf{n}_\omega$ is a n dimensional vector composed of gyroscopes' noise, and $\mathbf{z}$ is the $2n\times 1$ vector including measurements from each redundant sensors. With the known Gaussian distributed covariance matrix of measurement vector $\mathbf{R}$, the log likelihood function to be maximized is described as

$$L(\boldsymbol{\omega},\mathbf{f}) = -\frac{1}{2}\left\|\mathbf{z}-\mathbf{M}(\boldsymbol{\omega},\mathbf{d})-\mathbf{H}\mathbf{f}\right\|^2_{\mathbf{R}^{-1}} + c \tag{4.13}$$

where c is a constant and $\|\mathbf{x}\|^2_{\mathbf{A}} = \mathbf{x}^{\mathrm{T}}\mathbf{A}\mathbf{x}$.

As the angular rate and linear acceleration is divided separately in Eq. (4.12), the measurement equation is partially linear. Assuming that the lever arm vectors are known with sufficient accuracy, estimation of $\mathbf{f}$ that maximize the log likelihood may be derived when the specific estimate of angular rate $\boldsymbol{\omega}'$ is given, which can be properly set by applying conventional least square on Eq. (3.3). That is,

$$\hat{\mathbf{f}}(\boldsymbol{\omega}') = (\mathbf{H}^{\mathrm{T}}\mathbf{R}^{-1}\mathbf{H})^{-1}\mathbf{H}^{\mathrm{T}}\mathbf{R}^{-1}\left(\mathbf{z}-\mathbf{M}(\boldsymbol{\omega}',\mathbf{d})\right) \tag{4.14}$$

By substituting Eq. (4.14) into Eq. (4.13), the concentrated likelihood to be maximized with respect to angular rate can be described as

$$L(\boldsymbol{\omega}) = -\frac{1}{2}\left\|\mathbf{z}-\mathbf{M}(\boldsymbol{\omega},\mathbf{d})\right\|^2_{\mathbf{P}} + c \tag{4.15}$$

Therefore, the estimation of $\boldsymbol{\omega}$ that maximize Eq. (4.15) is completed by using Gauss-Newton algorithm [29], where the process is conducted numerically:

$$\hat{\boldsymbol{\omega}}_{k+1} = \hat{\boldsymbol{\omega}}_k + \left(\mathbf{J}^{\mathrm{T}}_{\mathbf{M}}\mathbf{P}\mathbf{J}_{\mathbf{M}}\right)^{-1}\mathbf{J}^{\mathrm{T}}_{\mathbf{M}}\mathbf{P}\left(\mathbf{z}-\mathbf{M}(\hat{\boldsymbol{\omega}}_k)\right) \tag{4.16}$$

where

$$\mathbf{P} = \mathbf{R}^{-1} - \mathbf{R}^{-1}\mathbf{H}(\mathbf{H}^{\mathrm{T}}\mathbf{R}^{-1}\mathbf{H})^{-1}\mathbf{H}^{\mathrm{T}}\mathbf{R}^{-1} \tag{4.17}$$

$$\mathbf{J}_{\mathbf{M}} = \frac{\partial \mathbf{M}}{\partial \boldsymbol{\omega}} = \begin{bmatrix} \mathbf{h}_1^{\mathrm{T}} \left(\boldsymbol{\Omega}_{\mathbf{d}_1 \times \boldsymbol{\omega}} + \boldsymbol{\Omega}_{\boldsymbol{\omega}}^{\mathrm{T}} \boldsymbol{\Omega}_{\mathbf{d}_1} \right) \\ \vdots \\ \mathbf{h}_n^{\mathrm{T}} \left(\boldsymbol{\Omega}_{\mathbf{d}_n \times \boldsymbol{\omega}} + \boldsymbol{\Omega}_{\boldsymbol{\omega}}^{\mathrm{T}} \boldsymbol{\Omega}_{\mathbf{d}_n} \right) \\ \mathbf{h}_1^{\mathrm{T}} \\ \vdots \\ \mathbf{h}_n^{\mathrm{T}} \end{bmatrix} \tag{4.18}$$

2) *Estimation of the linear acceleration*

Now complete the estimation by

$$\hat{\mathbf{f}} = \left(\mathbf{H}^{\mathrm{T}} \mathbf{R}^{-1} \mathbf{H} \right)^{-1} \mathbf{H}^{\mathrm{T}} \mathbf{R}^{-1} \left(\mathbf{z} - \mathbf{M}(\hat{\boldsymbol{\omega}}) \right) \tag{4.19}$$

where $\hat{\boldsymbol{\omega}}$ is the result of Eq. (4.16).

4.2.3 Performance analysis

The performance of the NLS suggested can be analyzed by deriving Fisher information matrix. For the parameter defined as $\boldsymbol{\theta} = \begin{bmatrix} \boldsymbol{\omega}^{\mathrm{T}} & \mathbf{f}^{\mathrm{T}} \end{bmatrix}^{\mathrm{T}}$, the Fisher information matrix $\mathcal{I}(\theta)$ of RIMU composed of n redundant accelerometers and n gyroscopes can be derived as

$$\begin{aligned} \mathcal{I}(\theta) &= \begin{bmatrix} \mathbf{J}_{\mathbf{M}} & \mathbf{H} \end{bmatrix}^{\mathrm{T}} \mathbf{R}^{-1} \begin{bmatrix} \mathbf{J}_{\mathbf{M}} & \mathbf{H} \end{bmatrix}^{\mathrm{T}} \\ &= \begin{bmatrix} \mathcal{I}_{11} & \mathcal{I}_{12} \\ \mathcal{I}_{21} & \mathcal{I}_{22} \end{bmatrix} \end{aligned} \tag{4.20}$$

where

$$\mathcal{I}_{11} = \frac{1}{\sigma_f^2} \sum_{i=1}^{n} \boldsymbol{\Omega}_i'^{\mathrm{T}} \mathbf{h}_i \mathbf{h}_i^{\mathrm{T}} \boldsymbol{\Omega}_i' + \frac{n}{3\sigma_\omega^2} \mathbf{I}_{3\times 3} \tag{4.21}$$

$$\mathcal{I}_{12} = \frac{1}{\sigma_f^2}\sum_{i=1}^{n} \boldsymbol{\Omega}_i'^{\mathrm{T}} \mathbf{h}_i \mathbf{h}_i^{\mathrm{T}} \tag{4.22}$$

$$\mathcal{I}_{21} = \frac{1}{\sigma_f^2}\sum_{i=1}^{n} \mathbf{h}_i \mathbf{h}_i^{\mathrm{T}} \boldsymbol{\Omega}_i' \tag{4.23}$$

$$\mathcal{I}_{22} = \frac{n}{3\sigma_f^2}\mathbf{I}_{3\times 3} \tag{4.24}$$

$$\boldsymbol{\Omega}_i' = \frac{1}{n}\sum_{i=1}^{n}\left(\boldsymbol{\Omega}_{\mathbf{d}_i\times\boldsymbol{\omega}} + \boldsymbol{\Omega}_{\boldsymbol{\omega}}^{\mathrm{T}}\boldsymbol{\Omega}_{\mathbf{d}_i}\right). \tag{4.25}$$

Using the Schur complement, the information related to angular rates can be expressed as

$$\begin{aligned}\mathcal{I}_{\omega} &= \mathcal{I}_{11} - \mathcal{I}_{12}\mathcal{I}_{22}^{-1}\mathcal{I}_{21} \\ &= \frac{n}{3\sigma_{\omega}^2}\mathbf{I}_{3\times 3} + \frac{1}{\sigma_f^2}\left[\sum_{i=1}^{n}\boldsymbol{\Omega}_i'^{\mathrm{T}}\mathbf{h}_i\mathbf{h}_i^{\mathrm{T}}\boldsymbol{\Omega}_i' - \frac{3}{n}\left(\sum_{i=1}^{n}\boldsymbol{\Omega}_i'^{\mathrm{T}}\mathbf{h}_i\mathbf{h}_i^{\mathrm{T}}\right)\left(\sum_{i=1}^{n}\mathbf{h}_i\mathbf{h}_i^{\mathrm{T}}\boldsymbol{\Omega}_i'\right)\right]\end{aligned} \tag{4.26}$$

where σ_f and σ_{ω} is the noise level of the accelerometers and gyroscopes respectively, assuming that n accelerometers have a similar level of noise, and n gyroscopes do the same. It is not a simple task to expand Eq. (4.26), where there are n different 3-dimensional direction cosine vectors $\mathbf{h}_i$ in redundant configurations. In order to make the expansion easier, the lever arm vectors $\mathbf{d}_i$ which are set to be aligned with $\mathbf{h}_i$ as Figure 4.4, is assumed to have the length of 1cm with the assumption that the same level of angular rates is given to each RIMU body frame axis, that is $\omega_x = \omega_y = \omega_z = \omega$. Then, the Eq. (4.26) can be expressed as:

$$\mathcal{I}_{\omega} = \frac{n}{3\sigma_{\omega}^2}\mathbf{I}_{3\times 3} + \frac{4\omega^2}{\sigma_f^2}\begin{bmatrix} \mathcal{I}'_{11} & \bullet & \bullet \\ \bullet & \mathcal{I}'_{22} & \bullet \\ \bullet & \bullet & \mathcal{I}'_{33} \end{bmatrix} \tag{4.27}$$

where

$$\mathcal{I}'_{11} = \sum_{i=1}^{n}\left\{\left(h_{i,1}\mathbf{1}-\mathbf{h}_i\right)\cdot\mathbf{h}_i\right\}^2 - \frac{3}{n}\sum_{i=1}^{n}\sum_{j=1}^{n}\left(\mathbf{h}_i\cdot\mathbf{h}_j\right)\left\{\left(h_{i,1}\mathbf{1}-\mathbf{h}_i\right)\cdot\mathbf{h}_i\right\}\left\{\left(h_{j,1}\mathbf{1}-\mathbf{h}_j\right)\cdot\mathbf{h}_j\right\} \tag{4.28}$$

$$\mathcal{I}'_{22} = \sum_{i=1}^{n}\left\{\left(h_{i,2}\mathbf{1}-\mathbf{h}_i\right)\cdot\mathbf{h}_i\right\}^2 - \frac{3}{n}\sum_{i=1}^{n}\sum_{j=1}^{n}\left(\mathbf{h}_i\cdot\mathbf{h}_j\right)\left\{\left(h_{i,2}\mathbf{1}-\mathbf{h}_i\right)\cdot\mathbf{h}_i\right\}\left\{\left(h_{j,2}\mathbf{1}-\mathbf{h}_j\right)\cdot\mathbf{h}_j\right\} \tag{4.29}$$

$$\mathcal{I}'_{33} = \sum_{i=1}^{n}\left\{\left(h_{i,3}\mathbf{1}-\mathbf{h}_i\right)\cdot\mathbf{h}_i\right\}^2 - \frac{3}{n}\sum_{i=1}^{n}\sum_{j=1}^{n}\left(\mathbf{h}_i\cdot\mathbf{h}_j\right)\left\{\left(h_{i,3}\mathbf{1}-\mathbf{h}_i\right)\cdot\mathbf{h}_i\right\}\left\{\left(h_{j,3}\mathbf{1}-\mathbf{h}_j\right)\cdot\mathbf{h}_j\right\} \tag{4.30}$$

From Eq. (4.27), it can be deduced that when no angular motion is applied, where $\omega = 0$, there is no information gained from the accelerometers. In that case, the inverse of the Eq. (4.27), which is the indicator of the Cramér Rao lower Bound (CRLB), shows the same value of Eq. (3.1).

When the angular motion is applied, the amount of information is increased, and it is proportional inversely to the noise level of the acceleration. This means that when the RIMU is configured with the accelerometers with the better specification, the information gained from them will be increased. However, as the direction of each sensing axes is included in Eq. (4.28) to Eq. (4.30), the performance of the angular rate estimation in RIMU with accelerometers of lower noise will be sensitive to the misalignment. The effect of the misalignment is shown to be acceptable by simulation with the specification of MEMS grade IMU in 4.3.

Although the result of Eq. (4.28) through Eq. (4.30) is difficult to analyze

explicitly, the qualitative interpretation is possible noting that $\left(h_{i,1}\mathbf{1}-\mathbf{h}_i\right)\cdot\mathbf{h}_i$ in the first term have maximum value when $\mathbf{h}_i$ is perpendicular to the vector $\mathbf{1}$, where $\mathbf{1}$ is originated from the given angular motion where $\omega_x=\omega_y=\omega_z=\omega$, corresponding to the orientation of the rotation vector. This implies that maximum information can be acquired from the sensing axes that is normal to the rotation vector, where the lever arm effect is mostly magnified.

Although the information is reduced by the second term, but it is cumbersome and trivial to prove that its value is always smaller than the information gained as the reduction effect will be minimized with the increasing number of accelerometers, leading the direction of the sensing axes around rotation vector to be evenly distributed. The value of Eq. (4.28) to Eq. (4.30) can be confirmed to be a positive with the previously proposed RIMU configurations with various number of redundant sensors.

4.3 Simulation results

4.3.1 RIMU configuration

To confirm the effect of the proposed methods, the following scenario of the angular rate is simulated, where the maximum turning rate is about 180deg/s in each axis

$$\omega_x=\omega_y=\omega_z=\sum_{n=1}^{10}\frac{2}{2n-1}\sin\left(\frac{2\pi}{2.5}(2n-1)t\right) \tag{4.31}$$

Also, in order to clarify the performance difference when the turning motion is applied, there are 2.5 seconds of static segments at every 10 seconds, starting from

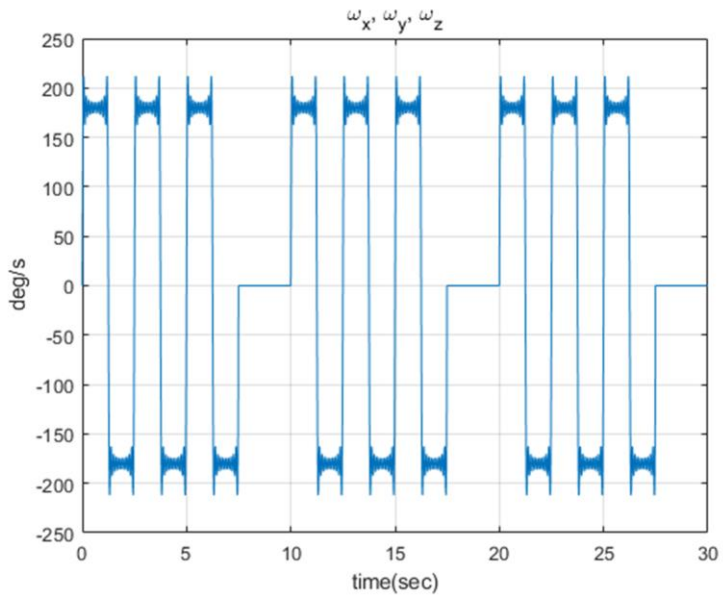

Figure 4.5: Turning motion of given RIMU configuration used in simulation

5s. The angular rate is described as Figure 4.5.

Two kinds of RIMU configuration is used in this simulation. One is the conventional configuration of Icosahedron [8], where all those lever arm vectors' directions are aligned with their sensing axes in order to minimize the lever arm effect as described in [6], but the length is determined to be 3cm without considering its physical feasibility to simplify the optimization problem. Based on the Icosahedron configuration, the proposed nonlinear least squares method will be compared to the conventional LS method.

The other configuration is composed of a pair of basis configuration where each of it has the sensing orientation of conical shape with five sensing axes, where the detail of it is described in Figure 4.3. All of the sensing axes are paired with a symmetric lever arm, which also has a length of 1cm. The two configurations are described in Figure 4.6.

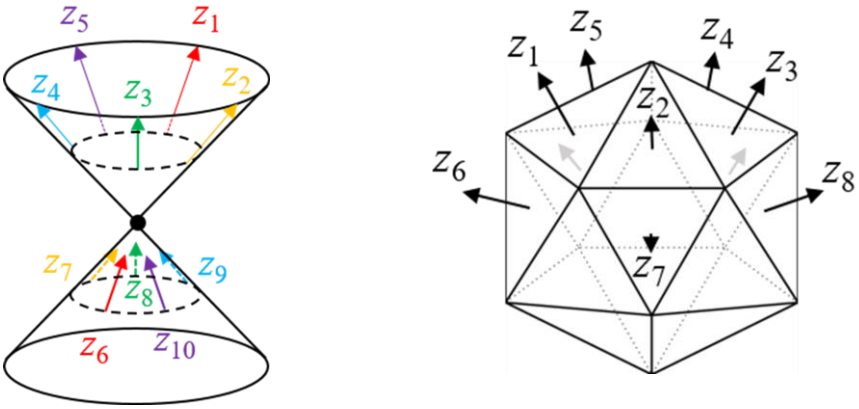

(a) Symmetric configuration (b) Conventional configuration

Figure 4.6: Two configurations of RIMU which have 10 sensing axes.

4.3.2 Navigation performance comparison

Based on the two configurations, three methods are compared with each other, where the conventional LS on Figure 4.6(a) and NLS on Figure 4.6(b) will be suggested method, and the conventional LS on Figure 4.6(b) will be compared to the former methods. The simulated sensor follows the specification of Bosch SMI130, which has the velocity random walk of $190ug/\sqrt{Hz}$, and angular random walk of $72\deg/\mathrm{hr}/\sqrt{Hz}$. The sampling rate is set to be $100Hz$. Assume that each of the sensing axe s is calibrated. The details of RIMU calibration can be referred to [30]-[32]. The following results are driven by 500 times of Monte Carlo simulations.

The RMSE of the estimated acceleration and angular rate is shown by Figure 4.7 and Figure 4.8. The result of the proposed methods is denoted as ‘symmetric LS’ and ‘NLS’ respectively. The black line stands for the noise level of the single

MEMS IMU, and the ‘analytic value’ of the noise corresponds to Eq. (4.8), where it corresponds to the result of conventional LS method without lever arm effect.

The noise driven by the lever arm effect is mitigated by the proposed methods, which can be clearly shown by the comparison of the segment with/without turning motion in Figure 4.7(a). Note that without the misalignment, the RMSE of symmetric configuration follows the analytic value. As described in 4.2.3, the estimation of angular rates gets more accuracy as the lever arm effect is applied, which can be confirmed in Figure 4.7(b). In other words, for the given amount of information from redundant sensors, NLS uses more information to estimate the angular rate. Therefore, the RMSE of acceleration of NLS is slightly increases more than that of symmetric LS.

To confirm the performance of the suggested methods under sever conditions that suffers from greater amount of lever arm effect, maximum turning rate about 360deg/s is applied for the same condition. Figure 4.8 shows that the proposed methods are more robust to the conventional methods under such conditions.

Based on the estimated acceleration and angular rate, the 3D position RMSE of the aforementioned methods with increasing length of lever arm and angular rates is shown in Figure 4.9. The 3D position RMSE of symmetric lever arm shows similar results to that of conventional method as it only has increased accuracy in acceleration estimates. Note that LS under symmetric lever arm does not include compensation. The position RMSE of NLS is greatly improves as it shows lower noise level both in linear acceleration and angular rates than that of conventional compensation method.

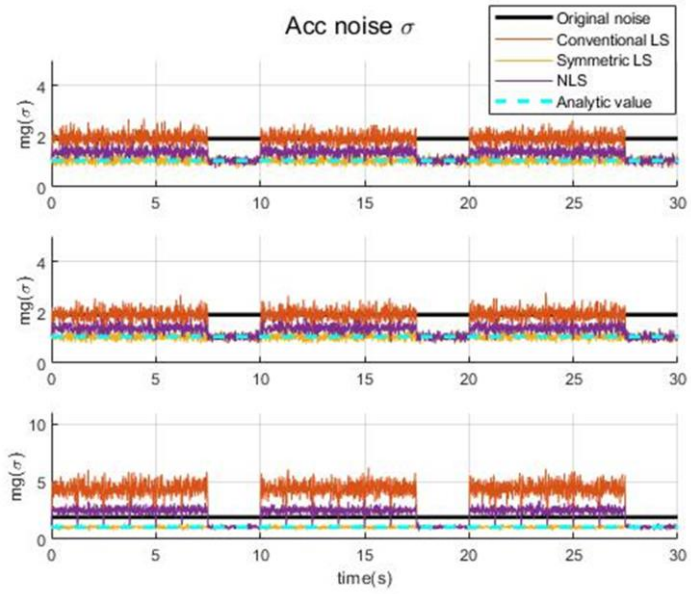

(a) Noise level of acceleration

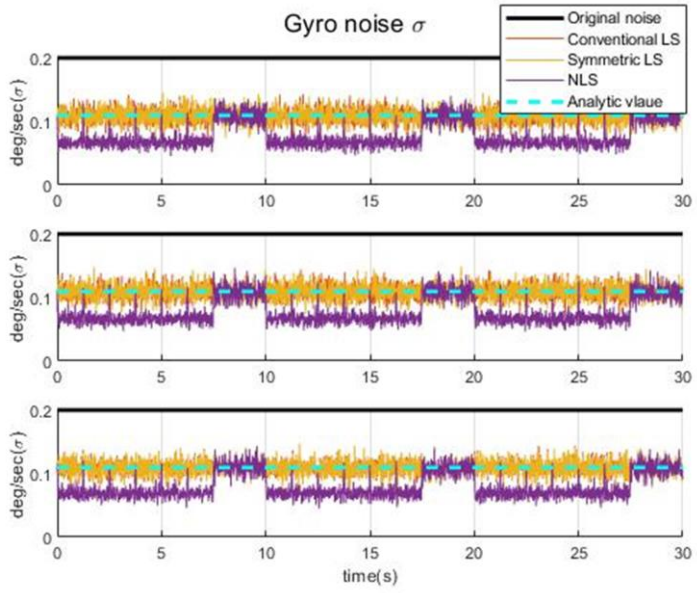

(b) Noise level of angular rate

Figure 4.7: RMSE of acceleration and angular rates

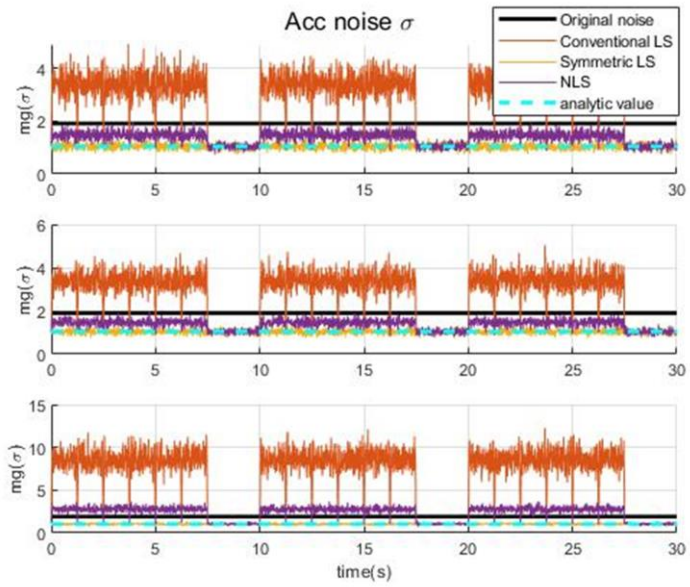

(a) Noise level of acceleration

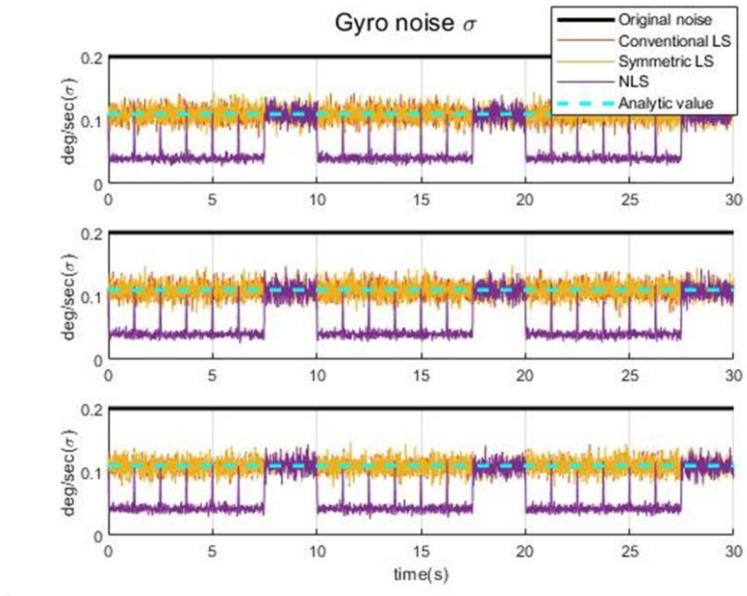

(b) Noise level of angular rate

Figure 4.8: RMSE of acceleration and angular rates under greater lever arm effect

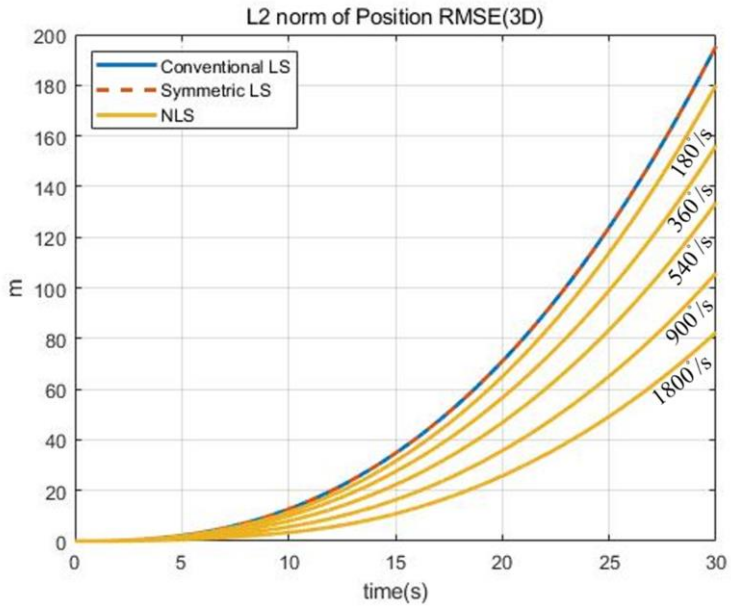

(a) Position RMSE according to the angular rate

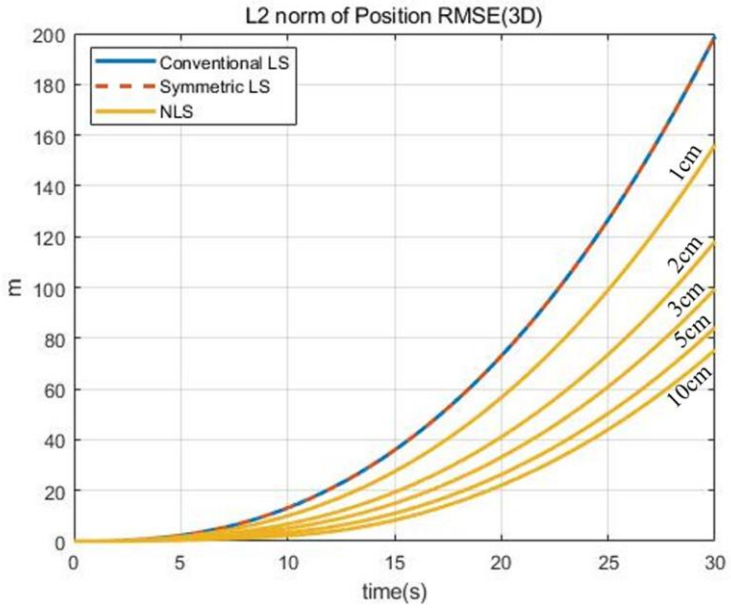

(b) Position RMSE according to the length of the lever arm

Figure 4.9: RMSE of 3D position

Meanwhile, most of the application of RIMU usually contains some amount of misalignment in each sensing axes. It can be referred to 4.1.3 and 4.2.3 that the suggested methods both includes orientation of sensing axes as a factor to their performance. Therefore, it can be deduced that the misalignment will act as an important factor. However, it is very complicated to verify the relationship between the magnitude of the misalignment in each axes and that of induced estimation error in each axes. Therefore, the effect of the misalignment is reviewed by adding misalignment in every axes with a certain amount of standard deviation.

It is confirmed by simulations that for the misalignment following the normal distribution with the standard deviation of 0.1 degree, the suggested methods still show enhanced performance than the conventional method. Figure 4.10 shows the mitigation of lever arm effect including misalignments in each redundant sensors under angular rate of 180deg/s in each axis in body frame. Figure 4.11 is under the same condition but angular rate of 360deg/s is applied.

The reduced amount of acceleration noise originated from the lever arm effect is calculated by averaging the difference of noise during the angular motion, where 100% reduction indicates that the noise level is as the same amount as Eq. (4.8). The reduced amount of angular rate noise by NLS is also calculated in the same manner, where 100% reduction indicate the situation where noise level is approximated to 0. The results are organized in Table 4.1 and Table 4.2, where the length of each lever arm is 3cm.

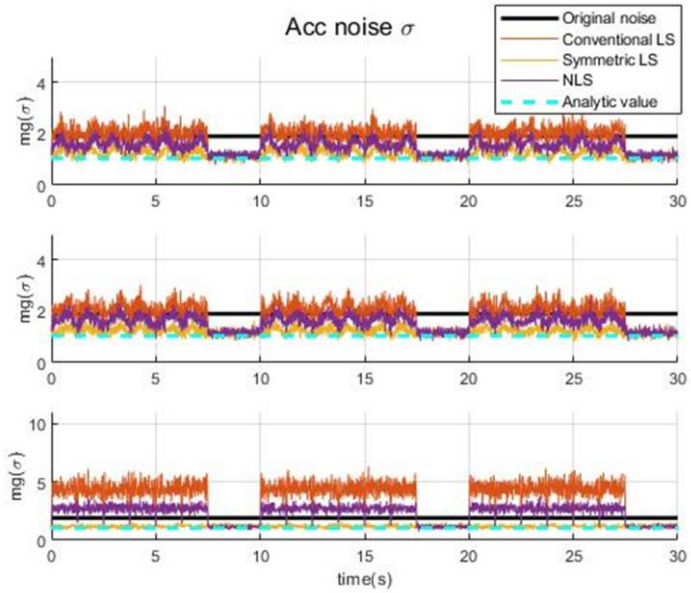

(a) Noise level of acceleration

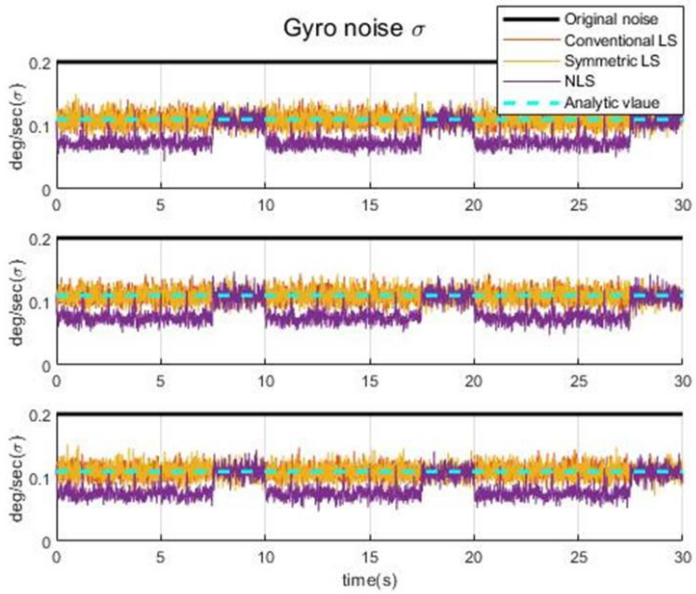

(b) Noise level of angular rate

Figure 4.10: RMSE of acceleration and angular rates with misalignments

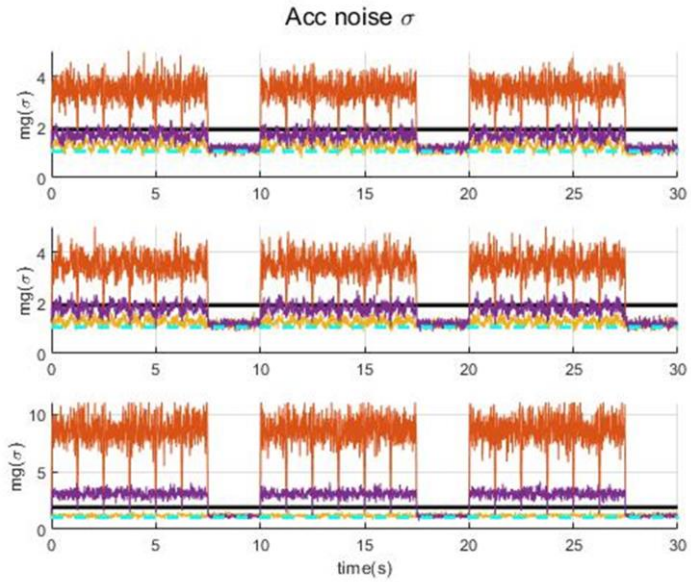

(a) Noise level of acceleration

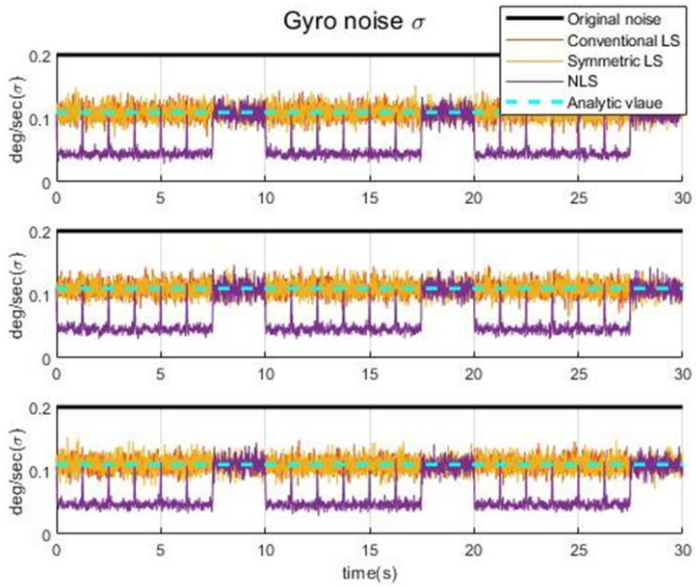

(b) Noise level of angular rate

Figure 4.11: RMSE of acceleration and angular rates under greater lever arm effect with misalignments

Table 4.1. Lever arm effect reduction rate with misalignment ~ $N(0,0.1\text{deg})$

Angular rate (deg/s)	180	360	540	900	1800
Symmetric LS	79.32%	91.11%	94.14%	95.72%	94.03%
NLS	47.04%	73.62%	82.55%	87.14%	78.91%

Table 4.2. Angular rate noise reduction rate with misalignment ~ $N(0,0.1\text{deg})$

Angular rate (deg/s)	180	360	540	900	1800
NLS	33.54%	58.25%	69.67%	78.51%	77.91%

Chapter 5

Conclusion

5.1.1 Conclusion and summary

In this thesis, two methods are proposed to mitigate the lever arm effect in RIMU where both methods focus to increase the accuracy in compensating centrifugal force with different approach. One is making multiple pairs of the sensing axes with the same orientation have lever arm vectors in opposite directions, maintaining the lever arm vectors aligned with sensing axes. Since the measured centrifugal force can be removed by simply summing all the measurements from redundant sensors, this method also reduces the computational burden for RIMU with multiple sensing axes where conventional method requires compensating unwanted specific force from each of the sensors.

The other method is using concentrated likelihood method-based nonlinear least squares to increase the estimation accuracy of angular rates. Since it utilizes information from accelerometers when angular motion is applied, not only it mitigate the lever arm effect, but also it uses lever arm effect to reduce the noise level of angular rates, contributing to the enhancement in overall inertial navigation performance.

Although the performance of the suggested methods is sensitive to the misalignment, the robustness is confirmed by simulations where every redundant

sensor are added with misalignments. The simulation was set that each sensors rotate with respect to a random rotation vector that cross the center of RIMU. The magnitude of the rotation follows a normal distribution with a standard deviation of 0.1deg.

In conclusion, for a RIMU consisting of low-grade gyroscopes, suggested methods are worth considering to mitigate lever arm effect that occurs during severe angular motion. Suggested methods are also useful when it is difficult to optimally assign a minimized length of the lever arm in a RIMU containing multiple sensing axes. Since first method requires doubling in total number of sensors and the second method requires additional computational effort, it is recommended that a designer should choose one of the proposed methods, considering between their benefits and drawbacks.

5.1.2 Future works

As the proposed methods show performance which is sensitive to the misalignment, the axis-wise quantitative error analysis based on the misalignment would contribute to understand the characteristics of estimation based on the various RIMU configurations.

Moreover, since the kinematic relation between lever arm and inertial measurements are well established, additional performance enhancement may be possible with the aid of the reasonable measurement model augmented by Kalman filter. In addition to the function that the estimation of the acceleration would not be affected when rotational motion is added, using nonlinear observer may reduce the noise level when rotational motion is not added.

Bibliography

[1] P. D. Groves, *Principles of GNSS, Inertial, and Multisensor Integrated Navigation Systems.* Boston, MA, USA: Artech House, 2008.

[2] D. H. Titterton and J. L. Weston, *Strapdown Inertial Navigation Technology,* 2nd ed. New York, NY, USA: IET, 2004.

[3] J. V. Harrison and E. G. Gai, "Evaluating sensor orientation for navigation performance and failure detection," *IEEE Trans. Aerosp. Eelctron. Syst.,* vol. AES-13, no. 6, pp. 631-643, Nov 1977.

[4] S. Sukkarieh, P. Gibbens, B. GrochLSky, K. Willis, and H. F. Durrant-Whyte, "A low-cost, redundant inertial measurement unit for unmanned air vehicles," *Int. J. Robot. Res.,* vol. 19, pp. 1089-1103, 2000.

[5] M. Sturza, "Skewed axis inertial sensor geometry for optimal performance," in *Proc. 8th AIAA/IEEE Digital Avionics Syst. Conf.,* Oct. 1988, pp. 128-135.

[6] J. W. Song and C. G. Park, "Optimal configuration of redundant inertial sensors considering lever arm effect," *IEEE Sensors Journal,* vol. 16, no. 9, pp. 3171-3180, 2015.

[7] A. J. Pejsa, "Optimum skewed redundant inertial navigators," *AIAA Journal,* vol. 12, no. 7, pp. 899-902, 1974.

[8] D. S. Shim and C. K. Yang, "Optimal configuration of redundant inertial sensors for navigation and FDI performance," *Sensors,* vol. 10, no. 7, pp. 6497-6512, 2010.

[9] J. Cheng, J. Dong, R. J. Landry, and D. Chen, “A novel optimal configuration form redundant MEMS inertial sensors based on the orthogonal rotation method,” *Sensors*, vol. 14, no. 8, pp. 13661-13678, 2014..

[10] C. K. Yang and D. S. Shim, “Best sensor configuration and accommodation rule based on navigation performance for INS with seven inertial sensors,” *Sensors*, vol. 9, no. 11, pp. 8456-8472, 2009.

[11] M. Jafari and J. Roshanian, “Optimal redundant sensor configuration for accuracy and reliability increasing in space inertial navigation systems,” *J. Navigat.*, vol. 66, no. 2, pp. 199-208, 2013.

[12] N. Sahu, P. Babu, A. Kumar, and R. Bahi, “A novel algorithm for optimal placement of multiple inertial sensors to improve the sensing accuracy,” *IEEE Trans. Signal Process.*, vol. 68, no. 4, pp. 142-154, 2019.

[13] K. C. Daly, E. Gai, and J. V. Harrison, “Generalized likelihood test for FDI in redundant sensor configurations,” *J. Guid. Control. Dyn.*, vol. 2, no. 1, pp. 9-17, 1979.

[14] J. Cheng, X. Sun, and H. Mou, “A modified GLT double faults isolation approach based on MLE and RPV for six-gyro redundant SINS,” *IEEE Access*, vol. 7, pp. 5312-5332, 2018.

[15] T. Chien and M. B. Adams, “A sequential failure detection technique and its application,” *IEEE Trans. Automat. Contr.*, vol. 21, no. 5, pp. 750-757, 1976.

[16] J. P. Gilmore and R. A. Mckern, “A redundant strpadown inertial reference unit (SIRU),” *J. Spacecraft and Rockets*, vol. 9, no.1, pp. 39-47, 1972.

[17] J. E. Potter and J. C. Deckert, “Minimax failure detection and identification

in redundant gyro and accelerometer systems," *J. Spacecraft and Rockets*, vol. 10, no. 4, pp. 236-243, 1973.

[18] S. Guerrier, A. Waegli, J. Skaloud, and M. P. Victoria-Feser, "Fault detection and isolation in multiple MEMS-IMUs configurations," *IEEE Trans. Aerosp. Electron. Syst.*, vol. 48, no. 3, pp. 2015-2031, 2012.

[19] W. Lee and C. G. Park, "Double fault detection of cone-shaped redundant IMUs using wavelet transformation and EPSA," *Sensors*, vol. 14, no. 2, pp. 3428-3444, 2014.

[20] A. R. Schuler, A. Grammatikos, and K. A. Fegley, "Measuring rotational motion with linear accelerometers," *IEEE Trans. Aerosp. Electron. Syst.*, vol. AES-3, no. 3, pp. 465-472, May 1967.

[21] P. Cardou and J. Angeles, "Angular velocity estimation from the angular acceleration matrix," *J. Appl. Mech.*, vol. 75, 2008.

[22] M. Patcher, T. C. Welker, and R. E. Huffman Jr, "Gyro-Free INS theory," *Navigation*, vol. 60, no. 2, pp. 85-96, 2013.

[23] B. Zappa, G. Legnai, A. J. Van den Bogert, and R. Adamini, "On the number and placement of accelerometers for angular velocity and acceleration determination," *J. Dynamic Syst., Meas., Control*, vol. 123, no. 3, pp. 552-554, 2001.

[24] P. Schopp, H. Graf, M. Maurer, M. Romanovas, L. Klingbeil, and Y. Manoli, "Observing relative motion with three accelerometer triads," *IEEE Trans. Instrum. Meas.*, vol. 63, no. 12, pp. 3137-3151, 2014.

[25] J. O. Nilsson and I. Skog, "Inertial sensor arrays-A literature review," in *2016 European Navigation Conference (ENC)*, Helsinki, 2016, pp. 1-10

[26] P. Stoica and A. Nehorai, "On the concentrated stochastic likelihood

function in array signal processing," *Circuits Syst. Signal Process.*, vol. 14, no. 5, pp. 669-674, 1995.

[27] I. Skog, J. O. Nilsson, P. Handel, and A. Nehorai, "Inertial sensor arrays, maximum likelihood, and cramér-rao bound," *IEEE Trans. Signal Process.*, vol. 64, no. 16, pp. 4218-4227, 2016.

[28] B. Eisenberg and R. Sullivan, "Why is the sum of independent normal random variables normal?," *Mathematics Magazine*, vol. 81, no. 5, pp. 362-366, 2008.

[29] S. Kay, *Fundamentals of Statistical Signal Processing: Estimation Theory,* Englewood Cliffs, NJ, USA: Prentice-Hall, 1933.

[30] S. Y. Cho and C. G. Park, "A Calibration technique for a redundant IMU containing low-grade inertial sensors," *ETRI Journal*, vol. 27, no. 4, pp. 418-426. 2005.

[31] S. Y. Cho and C. G. Park, "Calibration of a redundant IMU," in *Proc. AIAA Guid., Navigat., Control Conf. Exhibit*, Aug. 2004.

[32] M. Jafari, M. Sahebjameyan, B. Moshiri, and T. A. Najafabadi, "Skew redundant MEMS IMU calibration using a Kalman filter," *Meas. Sci. Technol.*, vol. 26, no. 10, Oct. 2015, Art. no. 105002

[33] J. E. Potter and M. C. Suman, "Thresholdless redundancy management with arrays of skewed insturuments," *NATO AGARDOGRAPH on Integrity Electron. Flight Control Syst.*, no. 224, pp. 15-11–15-25, 1977.

국문초록

본 논문에서는 중첩 관성 센서에서 발생하는 레버암 효과를 완화하기 위한 두 가지 새로운 기법을 제안한다. 중첩 관성 센서에서는 각 센서에 존재하는 레버암에 의해 회전 운동이 가해질 때 마다 오일러 힘이나 원심력과 같이 원치 않는 비력이 가속도 측정치에 섞여 추정 오차를 유발하게 된다. 따라서, 이를 해결하기 위해 제시된 최선의 방법은 길이가 최소화된 레버암에 의한 항 가속도 측정치로부터 보상한 값으로 추정하는 것이었다. 그러나, 보상하는 값이 노이즈가 섞인 각속도 추정치에 기반하기 때문에 기존 접근법은 추정 오차를 완전하게 제거할 수 없으며, 저가형 IMU와 같이 자이로스코프의 잡음 수준이 큰 경우에 대해 오차가 더 커지는 것을 확인할 수 있다. 이러한 문제를 해결하기 위해, 레버암 벡터를 특정한 형태로 배치시키거나 집중 우도 방법에 기반한 비선형 최소 자승 방식을 사용하여 추정 오차를 제거할 수 있는 방식을 제안한다. 제안된 방법에 따르면, 레버암의 대칭적인 배치 형태를 사용하거나 가속도계의 정보를 사용하여 각속도의 추정 오차를 우선적으로 줄여 궁극적으로 가속도 추정에 사용하는 보상하는 값의 정확도를 높이는 방식으로 레버암 효과를 줄일 수 있다. 또한, 제안된 방법은 각각 연산량의 효율성과 전반적인 관성항법 성능의 향상에서 추가적인 이점이 있다. 제안한 방식의 효과는 비정렬 오차를 포함한 시뮬레이션으로 검증하였다.

주요어: 관성항법, 중첩 관성센서, 레버암, 집중 우도 방식, 최적 항법 성능
학번: 2019-29291